Journal of Asian Earth Sciences 42 (2011) 1048–1065

Contents lists available at ScienceDirect

Journal of Asian Earth Sciences

journal homepage: www.elsevier.com/locate/jseaes

Cooling paths of the NE China crust during the Mesozoic extensional tectonics: Example from the south-Liaodong peninsula metamorphic core complex

Wei Lin [a,*], Patrick Monié [b], Michel Faure [c], Urs Schärer [d], Yonghong Shi [e], Nicole Le Breton [c], Qingchen Wang [a]

[a] State Key Laboratory of Lithospheric Evolution, Institute of Geology and Geophysics, Chinese Academy of Sciences, Beijing 100029, China
[b] Géosciences Montpellier, UMR-CNRS 5243, Université de Montpellier 2, Pl. E.-Bataillon, F-34095 Montpellier Cedex, France
[c] Institut des Sciences de la Terre d'Orléans, UMR-CNRS 6113, Campus Géosciences, Université d'Orléans, F-45067 Orléans Cedex 2, France
[d] Université de Nice-Sophia Antipolis, CNRS-UMR 6526, Parc Valrose, F-06108 Nice, France
[e] Department of Geology, School of Resource and Environment Engineering, Hefei University of Technology, Tunxi Road 193, Hefei, Anhui Province 230009, China

ARTICLE INFO

Article history:
Available online 18 November 2010

Keywords:
Metamorphic core complex
Cooling paths
Radiometric ages
Crustal extension
Lithospheric removal
North China Craton

ABSTRACT

The south-Liaodong peninsula massif is the easternmost Mesozoic metamorphic core complex, recognized in Eastern China. It provides a good example of the combination of ductile shearing, syn-kinematic plutonism and polyphase exhumation. The Jurassic granodioritic plutons, located at the footwall of the detachment normal fault, and dated here at ca 160 Ma, recorded two different phases of cooling. A slow cooling regime of about 3–10 °C/my prevailing before 122 Ma, was followed by a significant increase in cooling rate of about 40–55 °C/my after that time. By contrast, a single fast cooling path was recorded by the Cretaceous monzogranite situated in the footwall of the detachment normal fault. This result indicates that the Jurassic and Cretaceous plutons recorded different exhumation processes: a Jurassic slow or negligible exhumation and a Cretaceous fast one assisted by normal faulting. These two cooling stages correspond to distinct geodynamic processes during the Jurassic and Cretaceous. Extensional tectonics seems not significant before Early Cretaceous. The second stage, dominated by an extensional regime which develops after ca 120 Ma, is tentatively correlated to the lithosphere removal of the North China Craton.

© 2010 Elsevier Ltd. All rights reserved.

1. Introduction

The eastern part of north China represents an important tectonic element of the North China Craton (NCC). It is composed of several Archean blocks assembled during Early Paleoproterozoic times (Kusky and Li, 2003; Zhao et al., 2005; Faure et al., 2007; Trap et al., 2007) and covered by Meso and Neoproterozoic sediments (SBGMR, 1989; HBGMR, 1989). During the Late Paleozoic to Early Mesozoic, the tectonic evolution of the NCC was essentially located along its margins (Yin and Nie, 1993, 1996; Zhai et al., 2004). Along its southern border, the Qinling–Dabie–Sulu orogenic belt (Fig. 1A) corresponds to the collision zone between the NCC and the South China Block (SCB). As indicated by structural and metamorphic studies of UHP rocks, the lithosphere convergence accommodated more than 200 km of north-directed continental subduction (Mattauer et al., 1985; Hacker et al., 1998, 2006; Faure et al., 2003a,b; and references therein; Fig. 1A). To the north, the Central Asian Orogenic Belt (CAOB, Fig. 1A) corresponds to the successive accretions and collisions between the NCC and the intra-oceanic arcs and continental micro-blocks around the Siberian Craton during late Permian to Early Triassic times (Wang and Liu, 1986; Lamb and Badarch, 1997; Sengor and Natal'in, 1996; Xiao et al., 2003; Shang, 2004; Lin et al., 2008a).

Recently, the geology of the NCC has attracted great attention because of the coexistence of Ordovician diamondiferous kimberlites, Mesozoic lamprophyre-basalt and Cenozoic basalts in this craton, especially in the western part of Shandong province and in the South of Liaodong Peninsula. Silicate inclusions in diamonds, peridotites and disaggregated minerals in Ordovician kimberlites indicate the presence of a thick (~200 km), cold and refractory lithospheric keel beneath the NCC prior to the Paleozoic (Griffin et al., 1998; Xu, 2001). Based on geophysical data and petrological studies of mantle xenoliths from Late Mesozoic to Early Cenozoic basalts, it has been argued that the present lithosphere thickness lies between 120 km and 70 km (Fan and Menzies, 1992; Menzies et al., 1993; Menzies and Xu, 1998; Griffin et al., 1998; Zhang and Zheng, 2003; Deng et al., 2004; Zhang, 2005). This means that, during the Late Mesozoic (Griffin et al., 1998) or Cenozoic (Menzies et al., 1993), the lithosphere was thinned by more than 80 km.

At the crustal level, lithospheric thinning is accommodated by extensional tectonics represented by ductile and brittle normal

* Corresponding author. Tel.: +86 10 82998546; fax: +86 10 62010846.
E-mail address: linwei@mail.iggcas.ac.cn (W. Lin).

1367-9120/$ - see front matter © 2010 Elsevier Ltd. All rights reserved.
doi:10.1016/j.jseaes.2010.09.007

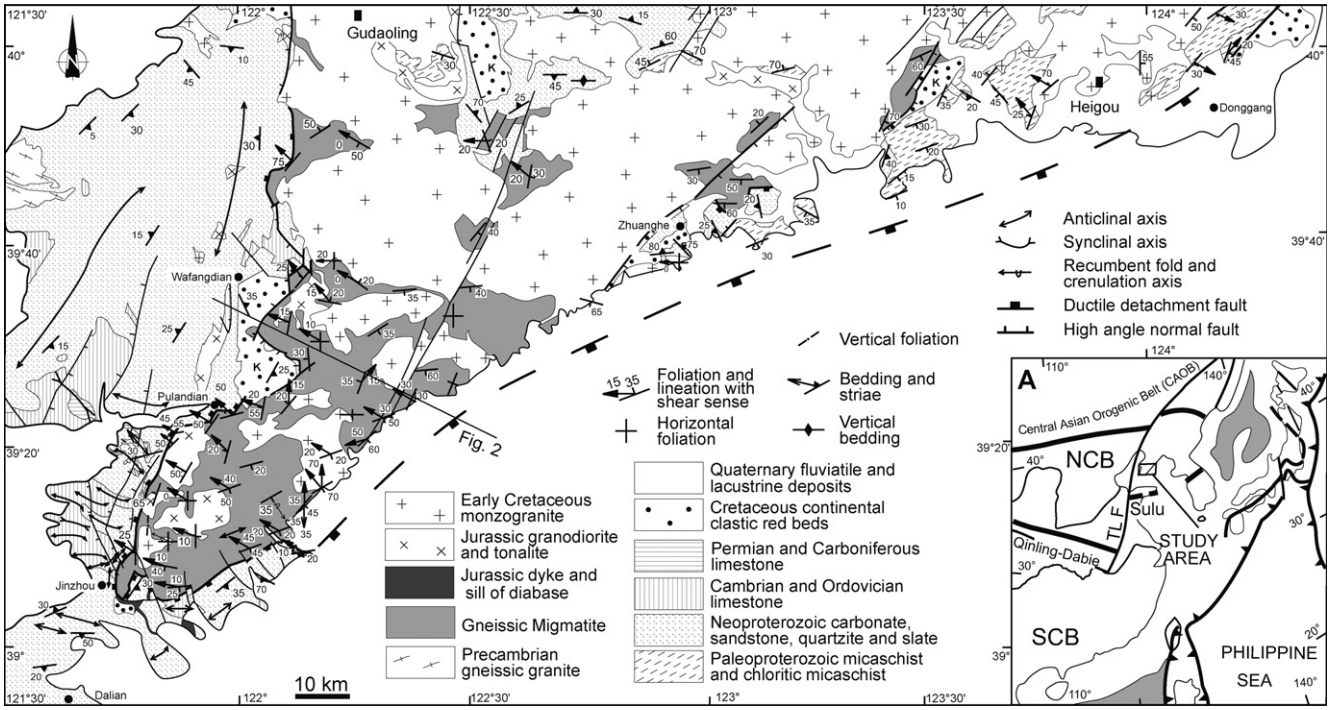

Fig. 1. Regional-scale structural map of the south-Liaodong peninsula massif. Inset shows the location of study area within the broader context of East Asia (modified from Lin et al., 2008b). NCB: North China Block; SCB: South China Block.

faulting active during the Cretaceous. This Late Mesozoic phase of extension occurred coevally with volumetrically important Cretaceous magmatism extending more than 4000 km, from the Okhotsk Sea in the North to Vietnam in the South (Zorin, 1999; Ren et al., 2002; Meng, 2003; Wu et al., 2005a). In East China, rift basins and related metamorphic complexes were recognized very early, even before the development of plate tectonics (Huang, 1945). Several models have been proposed to interpret the Mesozoic evolution of the NCC, involving processes such as rifting (Tian et al., 1992), mantle plume (Deng et al., 1998, 2004), thermal and chemical erosion of the lithospheric mantle (Xu, 1999, 2001), basaltic underplating (Zhang and Sun, 2002), mantle delamination (Gao et al., 1998, 2002) and subduction induced rollback (Ren et al., 2002). Both the exact timing and the processes of NCC thinning remain disputed. In NE China, the south-Liaodong peninsula massif has been recognized as a Cretaceous metamorphic core complex (MCC) with abundant plutonic rocks (e.g. Yin and Nie, 1993; Liu et al., 2005; Yang et al., 2007b; Lin et al., 2008b and references therein). Recently, a thermochronological study argued that the south-Liaodong peninsula massif experienced a fast cooling in Late Cretaceous between 120 and 107 Ma (i.e. Yang et al., 2007b). However, this study did not consider the Jurassic granodioritic plutons dated in the same area at 174–173 Ma on zircon by laser ablation ICP-MS method (Wu et al., 2005b). Therefore, a $^{40}Ar/^{39}Ar$ and U/Pb thermochronological study has been undertaken from undeformed, and deformed (foliated and mylonitized) granitoids, and their gneissic country rocks of the south-Liaodong peninsula massif, using a suite of minerals with different closure temperatures. The combination of the previous results with the new ones allows us to discuss the possible cooling path experienced by this MCC.

2. Geological framework of south-Liaodong peninsula massif

In the Liaoning Province of NE China, the south-Liaodong peninsula massif (Fig. 1) is composed of metamorphic and magmatic rocks, with Archean and Paleoproterozoic rocks occupying about half of the area (Yin and Nie, 1996; Lu et al., 2004; Faure et al., 2004; Li et al., 2005). Neoproterozoic and Paleozoic sediments overlie metamorphic rocks, which are intruded by Mesozoic granitoids (Wu et al., 2005a,b; Yang et al., 2007a,b,c). Mesozoic to Cenozoic terrigeneous rocks occur in fault-bounded troughs, suggesting basin formation related to extension (Allen et al., 1997; Okada, 1999; Ren et al., 2002). Structurally, the south-Liaodong peninsula massif is a Cretaceous asymmetric metamorphic core complex (MCC) called either the "Liaonan MCC" or "south-Liaodong peninsula" MCC with a NE–SW trending long axis (Fig. 1; Liu et al., 2005; Yang et al., 2007b; Lin et al., 2008b and references therein). It consists of three litho-tectonic units namely: (1) a gneissic migmatite unit, (2) a Paleo- to Mesoproterozoic micaschist and slate unit, and (3) a Neoproterozoic to Mesozoic sedimentary cover.

The south-Liaodong peninsula MCC shows NW-SE trending extension direction (Liu et al., 2005; Yang et al., 2007b; Lin et al., 2008b). The Paleoproterozoic gneisses and foliated migmatite that form the lower plate of the MCC are heterogeneously deformed with a relatively weakly foliated core and a mylonitic shear zone at the margin. The dome boundary is a low-angle ductile detachment normal fault locally reworked by a brittle high-angle fault (Fig. 2). Two types of granitic plutons intrude the metamorphic series. Jurassic granodiorites are pervasively foliated, whereas Early Cretaceous syntectonic monzogranitic plutons are weakly foliated except where they are involved in the detachment fault. In this latter structure, the granitic rocks were converted to mylonite or ultramylonite. Kinematic shear criteria show a top-to-the-NW sense of movement along the detachment fault. As observed in the metamorphic core complexes of North America (e.g. Lister and Davis, 1989), the detachment fault of the south-Liaodong peninsula MCC is arched, due to syn-extensional folding around a NE-SW axis (Fig. 1). As a result, the SE dome limb appears as a top-to-the-NW thrust, which is in reality a folded normal fault. In the hanging wall of the detachment fault, the Neoproterozoic and Paleozoic sedimentary rocks are deformed by northwestward verging folds (Fig. 1; Lin et al., 2008b).

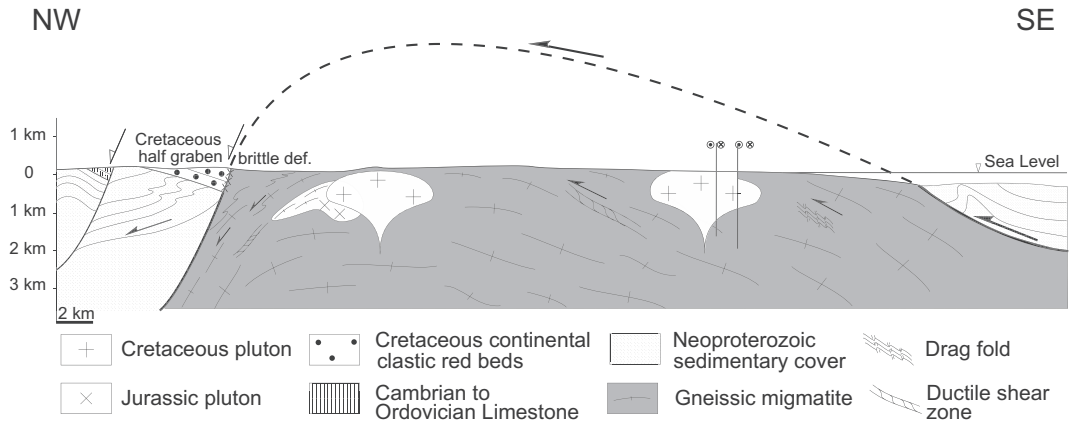

Fig. 2. Cross-sections though the south-Liaodong peninsula massif (location shown in Fig. 1) drawn parallel to the direction of the main mineral and stretching lineation (modified from Lin et al., 2008b).

Along the ductile detachment normal fault, several samples were collected in order to constrain the time of exhumation of the south-Liaodong peninsula MCC using the laser probe single grain step-heating $^{40}Ar/^{39}Ar$ method on biotite and amphibole and the U/Pb thermo-ionization mass spectrometry method on the titanite fraction. Combined with the previous geochronological work (Yin and Nie, 1996; Wu et al., 2005a,b; Yang et al., 2004, 2007b), we can establish the cooling history of south-Liaodong peninsula MCC.

3. Geochronology

3.1. Previous geochronological data

In the south-Liaodong peninsula MCC, several previous studies provide different time constraints. Different type of granite, migmatite, metamorphic rocks and mylonite are well dated radiometrically. Zircon U–Pb, LA-ICP-MS dating of medium to fine-grained monzogranites and biotite–granites yield ages in the range of 135–110 Ma (Fig. 3; Wu et al., 2005a). Meanwhile, at the northwestern part of the massif, 150–180 Ma old, biotite–hornblende granodiorites and tonalites were also dated (Wu et al., 2005b; Yang et al., 2007a). Zircon from the gneissic, even mylonitic, migmatite reveals a range of ages from 2518 to 2457 Ma (LA-ICP-MS, Lu et al., 2004). In order to reveal the age and the processes of the exhumation of this massif, muscovite, hornblende, biotite, and K-feldspar from mylonitic migmatite, deformed mafic dyke and granitic rocks were dated (Yin and Nie, 1996; Yang et al., 2004, 2007b). The$^{40}Ar/^{39}Ar$ ages, distributing in two clusters between 113–110 Ma and 125–105 Ma, were interpreted as those of exhumation and cooling, respectively.

In order to reveal more detail of the tectonic processes of the south-Liaodong peninsula MCC, especially considering the exhumation of Jurassic granodioritic plutons, nine mineral samples have been dated with the $^{40}Ar/^{39}Ar$ method and a granodioritic intrusion was collected for titanite dating by the U–Pb method.

3.1.1. $^{40}Ar/^{39}Ar$ dating

A total of 9 mineral samples have been dated with the laser probe $^{40}Ar/^{39}Ar$ method using a single grain step-heating procedure (Table 1). Samples were taken from both the northern and southern sides of the dome in order to place age constraints on the top to the NW shearing (Fig. 1). The dated rocks are gneissic and mylonitic migmatites (LN66 and LN93), deformed amphibolites (LN59, LN70), orthogneiss (LN56, LN71), mylonitized granodiorite (LN82, 83, 85) within the detachment zone, and undeformed biotite granite (LN110) from the dome core (Fig. 3). Table 1 summarizes the location, lithology, dated minerals, state of deformation and $^{40}Ar/^{39}Ar$ results for each sample.

Dating was performed on 0.5–1 mm sized minerals separated under a binocular microscope after coarse rock crushing. These minerals were packed in aluminum foil for fast neutron irradiation for 60 h in the McMaster nuclear reactor together with several MMHb1 hornblende flux monitors (520.4 ± 1.7 Ma; Samson and Alexander, 1987). After irradiation, the minerals were placed on a copper plate inside an UHV extraction system and baked for 48 h at 200 °C. Step-heating experiments were conducted on single grains with the laser operating in the continuous mode, by increasing its power at each step. There was no direct control of the temperature applied to the samples. Only their infrared color change was checked with a camera placed above the sample chamber. The analytical device consists of: (a) a multiline continuous 6 W argon-ion Lexel 3500 laser; (b) a beam shutter for selection of exposure times, typically 30 s for individual steps; (c) divergent and convergent lenses for definition of the beam diameter; (d) a small inlet line for the extraction and purification of gases; (e) a MAP 215–50 noble gas mass spectrometer. Each analysis involves 5 min for gas extraction and cleaning and 15 min for data acquisition by peak switching from mass 40 to mass 36. System blanks were evaluated every three analyses and ranged from 3×10^{-12} cc for ^{40}Ar to 4×10^{-14} cc for ^{36}Ar. Ages and errors were calculated according to McDougall and Harrison (1999). Complete results are reported in Table 2 and illustrated as age spectra and reverse isochron plots. The quoted errors represent one sigma deviation and include uncertainty on the monitor age and its $^{40}Ar/^{39}Ar$ ratio. This uncertainty is considered in the calculation of the plateau and total age errors. Data have been also reported in $^{36}Ar/^{40}Ar$ vs. $^{39}Ar/^{40}Ar$ correlation plots and Table 1 compares the results given by the two methods of age evaluation.

Age spectra and reverse isochron plots of five biotites from gneissic migmatite, amphibolite, orthogneiss, mylonitic, and undeformed granite are shown in Fig. 4a–e and a′–e′. These spectra are flat for a large percentage of the argon released. Most of them do not satisfy the strict definition of a plateau age in the sense of Fleck et al. (1977), i.e. 3 or more contiguous heating steps comprising 50% or more of the ^{39}Ar released and overlapping at the two sigma confidence level. This is partly due to the fact that the dated minerals were probably contaminated by the presence of optically undetectable minute inclusions, by inherited argon or by alteration products. Therefore, and more frequently for biotite, age spectra display small internal age variations that probably result from

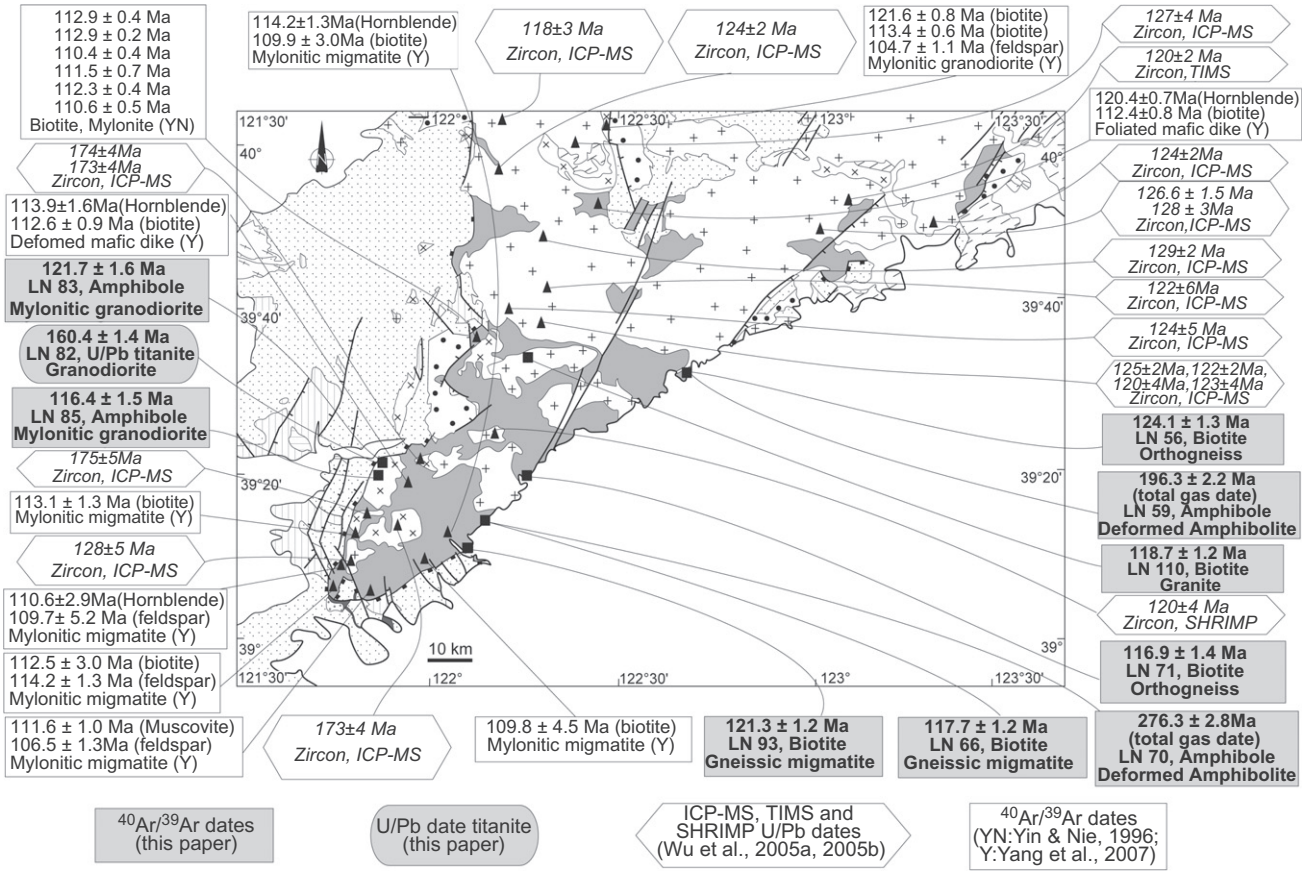

Fig. 3. Map of the south-Liaodong peninsula massif showing the available radiometric data. $^{40}Ar/^{39}Ar$ ages of biotite and amphibole and U/Pb age of titanite are given in this paper. ICP-MS, SHRIMP and TIMS zircon ages are from Wu et al. (2005a,b), Ar-biotite and muscovite ages from Yin and Nie (1996) and K-feldspar ages from Yang et al. (2007b). Symbols and captions in the map are the same as in Fig. 1.

Table 1
Summary of the samples dated by the $^{40}Ar/^{39}Ar$ method.

Sample	Rock type	Coordinates	Analyzed mineral	Total age	Plateau age	Intercept age	(40Ar/36Ar)i	MSWD
LN56	Orthogneiss	N 39°32.21′; E 122°41.73′	Biotite	127.2 ± 1.2	124.1 ± 1.3	124.9 ± 1.2	261 ± 30	1.29
LN59	Amphibolite restite	N 39°32.21′; E 122°41.73′	Amphibole	196.3 ± 2.2	–	–	–	–
LN66	Gneissic migmatite	N 39°15.89′; E 122°12.46′	Biotite	118.2 ± 1.1	117.7 ± 1.2	118.3 ± 1.1	272 ± 26	0.46
LN70	Amphibolite restite	N 39°15.89′; E 122°12.46′	Amphibole	276.3 ± 2.8	–	–	–	–
LN71	Orthogneiss	N 39°16.68′; E 122°14.14′	Biotite	116.9 ± 1.4	116.9 ± 1.4	118.1 ± 1.3	288 ± 8	1.49
LN83	Mylonitic granodiorite	N 39°21.93′; E 121°55.63′	Amphibole	121.3 ± 1.3	121.7 ± 1.6	117.5 ± 1.8	456 ± 129	2.55
LN85	Gneissic granodiorite	N 39°20.43′; E 121°53.94′	Amphibole	113.6 ± 1.3	116.4 ± 1.5	115.1 ± 1.5	341 ± 93	0.96
LN93	Mylonitized amphibolite	N 39°10.23′; E 122°05.52′	Biotite	120.9 ± 1.2	121.3 ± 1.2	120.4 ± 1.2	360 ± 24	1.54
LN110	Undeformed Cretaceous monzogranite	N 39°34.47′; E 122°15.14′	Biotite	118.0 ± 1.0	118.7 ± 1.2	119.2 ± 1.2	275 ± 8	2.96

Sample description

LN56: Southeastern border of MCC. Mylonitized to ultramylonitized Archean gneiss with green–brown biotite, microcrystalline quartz and quartz ribbons, feldspar and amphibole clasts and calcite. Biotite has a synkinematic habit.

LN59: Southeastern border of MCC. Amphibolite boudin with blue–green amphibole, quartz, epidote and titanite. A single generation of amphibole defines the foliation.

LN66: Southeastern border of MCC. Strongly mylonitized Archean gneissic migmatite with syn-kinematic green–brown biotite, feldspar, microcrystalline quartz and quartz ribbons and epidote.

LN70: Southeastern border of MCC. Unfoliated amphibolite boudin in orthogneiss with a single generation of blue–green amphibole, quartz, epidote and titanite.

LN71: Southeastern border of MCC. Partially mylonitized orthogneiss. In thin section, partially chloritized biotite coexists with quartz, feldspar, epidote, garnet and titanite.

LN83: Northwestern border of MCC. Weakly mylonitized granodiorite with magmatic quartz, feldspar, scarce chloritized biotite, amphibole and titanite. In thin section, quartz is recrystallized and partially oriented. Grains of amphibole do not show any evidence of recrystallization at their rim.

LN85: Northwestern border of MCC. Strongly mylonitized granodiorite with green biotite, amphibole, feldspar, quartz ribbons and epidote. Both clastic and synkinematic amphiboles coexist in this sample

LN93: Southeastern border of MCC. Mylonitized felsic gneiss with syn-kinematic green–brown biotite, quartz ribbons, abundant epidote, prophyroclasts of plagioclase and garnet.

LN110: Center of MCC. Undeformed Cretaceous monzogranite with biotite, quartz and K-feldspar.

degassing of different textural and chemical microdomains. For the least discordant portion of these spectra, we calculate pseudo-plateau ages that are statistically similar to the intercept ages obtained in the $^{36}Ar/^{40}Ar$ vs. $^{39}Ar/^{40}Ar$ correlation plot (Table 1) with initial $^{36}Ar/^{40}Ar$ ratios that do not significantly deviate from the present day atmospheric value (1/295.5). These

Table 2
$^{40}Ar/^{39}Ar$ analytical data.

N°	$^{40}Ar^{*}/^{39}Ar$	$^{36}Ar/^{40}Ar \times 1000$	$^{39}Ar/^{40}Ar$	$^{37}Ar/^{39}Ar$	% ^{39}Ar	% Atm	Age	Error
LN56 biotite		*J = 0.011,781*						
1	20.684	2.421	0.0137	0.455	0.4	71.5	393.5	20.2
2	7.956	2.151	0.0457	0.196	1.6	63.5	161.7	7.2
3	6.073	1.268	0.1029	0.012	4.8	37.4	124.7	2.5
4	6.154	0.651	0.1312	0.011	9.8	19.2	126.3	1.6
5	6.568	0.406	0.1339	0.025	13.5	12.0	134.5	2.0
6	6.488	0.354	0.1379	0.015	17.8	10.4	132.9	1.6
7	6.284	0.306	0.1446	0.001	23.0	9.0	128.9	1.0
8	6.165	0.325	0.1464	0.004	28.2	9.6	126.5	1.4
9	6.016	0.321	0.1504	0.018	32.4	9.5	123.6	4.0
10	6.184	0.320	0.1463	0.000	37.5	9.4	126.9	2.2
11	6.022	0.368	0.1479	0.021	41.5	10.8	123.7	1.6
12	5.999	0.276	0.1530	0.012	46.1	8.1	123.2	2.1
13	5.927	0.286	0.1543	0.008	51.2	8.4	121.8	1.4
14	6.021	0.292	0.1517	0.032	56.1	8.6	123.7	1.4
15	5.996	0.290	0.1524	0.090	61.9	8.5	123.2	0.8
16	5.923	0.216	0.1579	0.136	66.6	6.3	121.7	1.0
17	6.007	0.212	0.1559	0.039	71.3	6.2	123.4	1.4
18	6.074	0.229	0.1534	0.071	76.2	6.7	124.7	1.4
19	6.140	0.245	0.1509	0.041	81.0	7.2	126.0	1.7
20	6.079	0.201	0.1546	0.034	86.6	5.9	124.8	1.2
21	6.027	0.159	0.1579	0.100	91.3	4.7	123.8	0.9
22	6.109	0.079	0.1597	0.069	98.9	2.3	125.4	0.7
23	6.428	0.109	0.1505	0.302	100.0	3.2	131.7	1.7
						Total age = 127.2 ± 1.2		
LN59 amphibole		*J = 0.011781*						
1	46.529	1.732	0.0104	2.268	0.6	51.1	788.6	25.1
2	17.709	1.604	0.0296	0.665	1.3	47.4	341.9	38.9
3	9.255	0.925	0.0785	0.154	2.2	27.3	186.7	21.9
4	15.818	0.152	0.0603	0.478	3.2	4.5	308.3	18.2
5	4.623	1.628	0.1121	2.155	4.6	48.1	95.7	14.5
6	5.868	0.081	0.1662	3.383	6.2	2.4	120.6	5.4
7	6.235	0.569	0.1333	4.486	9.0	16.8	127.9	7.9
8	6.808	0.156	0.1400	5.641	12.2	4.6	139.2	6.1
9	7.020	0.521	0.1205	7.685	18.7	15.3	143.4	4.5
10	7.345	0.490	0.1164	7.510	23.5	14.4	149.7	3.9
11	10.954	0.343	0.0820	7.849	32.9	10.1	219.0	2.2
12	12.917	0.120	0.0745	7.060	44.5	3.5	255.6	3.2
13	11.180	0.295	0.0815	7.707	62.7	8.7	223.2	2.6
14	8.118	0.053	0.1212	6.271	66.0	1.5	164.8	8.1
15	7.225	0.042	0.1366	5.012	67.6	1.2	147.4	17.3
16	6.529	0.024	0.1520	5.146	69.0	0.7	133.7	17.7
17	7.567	0.376	0.1174	8.140	71.9	11.1	154.1	11.3
18	8.121	0.562	0.1026	7.680	80.7	16.6	164.9	3.8
19	8.137	0.579	0.1018	5.552	84.1	17.1	165.2	5.0
20	8.092	0.385	0.1094	5.236	86.6	11.3	164.3	10.2
21	8.123	0.081	0.1201	5.638	89.0	2.4	164.9	5.2
22	9.901	0.056	0.0993	5.907	97.1	1.6	199.1	4.2
23	10.182	0.164	0.0934	9.056	100.0	4.8	204.4	3.3
						Total age = 196.3 ± 2.2		
LN66 biotite		*J = 0.011781*						
1	5.385	2.538	0.0464	0.044	0.5	75.0	111.0	10.7
2	6.262	0.971	0.1138	0.017	3.8	28.6	128.4	2.0
3	5.723	0.264	0.1610	0.001	18.2	7.8	117.7	0.6
4	5.724	0.108	0.1691	0.007	31.3	3.1	117.7	0.8
5	5.629	0.124	0.1711	0.004	37.7	3.6	115.9	1.5
6	5.731	0.091	0.1697	0.001	44.2	2.6	117.9	1.1
7	5.765	0.094	0.1685	0.003	50.4	2.7	118.6	1.1
8	5.721	0.140	0.1675	0.015	56.8	4.1	117.7	0.9
9	5.722	0.115	0.1687	0.001	61.9	3.4	117.7	1.8
10	5.788	0.041	0.1706	0.007	66.9	1.2	119.0	0.8
11	5.746	0.040	0.1719	0.007	71.8	1.1	118.2	0.8
12	5.763	0.021	0.1723	0.031	77.3	0.6	118.5	0.5
13	5.724	0.058	0.1716	0.017	83.1	1.7	117.8	0.9
14	5.680	0.016	0.1752	0.039	87.1	0.4	116.9	1.8
15	5.680	0.146	0.1684	0.049	90.2	4.3	116.9	1.3
16	5.756	0.026	0.1723	0.086	92.6	0.7	118.4	2.3
17	5.628	0.041	0.1754	0.097	94.2	1.2	115.8	3.6
18	5.893	0.080	0.1656	0.269	100.0	2.3	121.1	1.1
						Total age = 118.2 ± 1.1		

Table 2 (*continued*)

N°	$^{40}Ar^{*}/^{39}Ar$	$^{36}Ar/^{40}Ar \times 1000$	$^{39}Ar/^{40}Ar$	$^{37}Ar/^{39}Ar$	% ^{39}Ar	% Atm	Age	Error
LN70 amphibole		*J = 0.011781*						
1	187.575	0.152	0.005	5.309	0.0	4.5	2104.0	54.7
2	19.475	1.443	0.029	1.898	0.4	42.6	372.7	33.6
3	8.837	0.141	0.108	1.072	1.2	4.1	178.7	9.8
4	6.480	0.133	0.148	1.372	2.0	3.9	132.7	13.4
5	6.838	0.423	0.128	3.982	3.3	12.5	139.8	9.7
6	7.584	0.470	0.114	5.394	5.8	13.8	154.4	7.3
7	10.797	0.148	0.089	6.410	14.7	4.3	216.0	3.0
8	11.749	0.135	0.082	6.200	20.2	4.0	233.9	4.1
9	12.725	0.172	0.075	5.688	26.5	5.0	252.0	3.0
10	14.333	0.195	0.066	5.050	37.3	5.7	281.5	4.1
11	17.099	0.144	0.056	5.106	46.6	4.2	331.1	3.8
12	16.900	0.136	0.057	5.456	51.6	4.0	327.6	6.7
13	17.095	0.014	0.058	4.769	56.5	0.4	331.1	5.0
14	15.180	0.027	0.065	5.557	62.7	0.7	296.8	3.8
15	14.346	0.048	0.069	5.438	64.4	1.4	281.8	6.6
16	14.019	0.106	0.069	5.150	100.0	3.1	275.8	2.3
						Total age = 276.3 ± 2.8		
LN71 biotite		*J = 0.011781*						
1	5.649	1.356	0.1060	0.003	57.1	40.0	116.2	1.3
2	5.891	0.122	0.1636	0.016	62.6	3.6	121.1	2.4
3	5.760	0.221	0.1622	0.019	70.3	6.5	118.5	2.1
4	5.563	0.192	0.1694	0.021	78.1	5.6	114.5	2.3
5	5.837	0.001	0.1712	0.062	82.6	0.0	120.0	3.2
6	5.788	0.116	0.1667	0.042	86.6	3.4	119.0	3.5
7	5.474	0.283	0.1673	0.051	90.0	8.3	112.8	3.2
8	6.026	0.017	0.1649	0.010	92.9	0.5	123.8	3.5
9	5.572	0.185	0.1696	0.023	97.3	5.4	114.7	2.6
10	5.863	0.019	0.1694	0.033	100.0	0.5	120.5	3.4
						Total age = 116.9 ± 1.4		
LN83 amphibole		*J = 0.011781*						
1	42.714	0.303	0.0212	2.554	0.1	8.9	735.4	53.1
2	7.979	0.257	0.1157	3.864	0.7	7.6	162.1	14.1
3	5.513	0.448	0.1573	3.809	4.3	13.2	113.5	4.9
4	5.334	0.488	0.1603	3.901	7.9	14.4	110.0	3.9
5	5.444	0.631	0.1494	3.608	13.0	18.6	112.2	3.4
6	6.043	0.356	0.1480	3.768	21.6	10.5	124.1	2.0
7	5.969	0.091	0.1630	3.996	42.6	2.6	122.6	1.4
8	5.697	0.170	0.1666	3.574	59.5	5.0	117.2	1.2
9	5.708	0.251	0.1621	3.709	67.4	7.4	117.4	2.5
10	5.465	0.454	0.1584	3.836	69.7	13.4	112.6	5.4
11	5.594	0.083	0.1743	3.469	71.4	2.4	115.2	8.4
12	5.736	0.134	0.1673	3.790	72.1	3.9	118.0	18.3
13	6.113	0.214	0.1532	4.090	81.9	6.3	125.5	1.9
14	5.948	0.140	0.1611	3.785	100.0	4.1	122.2	2.5
						Total age = 121.3 ± 1.3		
LN85 amphibole		*J = 0.011781*						
1	4.646	2.542	0.0535	0.755	1.6	75.1	96.2	9.5
2	3.727	1.610	0.1406	0.386	4.7	47.5	77.5	4.8
3	5.497	0.923	0.1322	1.179	8.9	27.3	113.2	4.9
4	5.686	1.187	0.1141	0.790	11.4	35.0	117.0	4.6
5	6.001	0.426	0.1455	1.113	14.0	12.5	123.2	4.6
6	5.187	0.643	0.1561	2.123	17.6	19.0	107.0	4.4
7	5.311	0.341	0.1692	2.557	22.4	10.1	109.5	2.9
8	5.409	0.292	0.1688	2.332	26.9	8.6	111.5	2.4
9	5.411	0.370	0.1645	2.534	31.6	10.9	111.5	2.6
10	5.407	0.238	0.1719	2.363	36.3	7.0	111.4	2.3
11	5.641	0.331	0.1599	3.485	45.6	9.7	116.1	1.7
12	5.685	0.139	0.1685	3.982	74.8	4.1	117.0	1.7
13	5.548	0.141	0.1726	3.450	83.8	4.1	114.2	2.1
14	5.432	0.273	0.1691	2.919	88.0	8.0	111.9	3.1
15	5.736	0.084	0.1699	2.956	92.3	2.4	118.0	3.7
16	5.729	0.238	0.1622	2.404	97.7	7.0	117.9	2.6
17	5.929	0.151	0.1611	2.263	100.0	4.4	121.8	4.4
						Total age = 113.6 ± 1.3		
LN93 biotite		*J = 0.011781*						
1	3.214	3.280	0.0094	1.724	0.0	96.9	67.1	169.6
2	4.929	2.081	0.0780	0.046	5.1	61.4	101.9	3.1
3	6.078	0.568	0.1367	0.010	9.4	16.7	124.8	1.9

(*continued on next page*)

Table 2 (*continued*)

N°	$^{40}Ar^{*}/^{39}Ar$	$^{36}Ar/^{40}Ar \times 1000$	$^{39}Ar/^{40}Ar$	$^{37}Ar/^{39}Ar$	% ^{39}Ar	% Atm	Age	Error
4	6.113	0.492	0.1397	0.016	18.2	14.5	125.5	1.1
5	6.062	0.366	0.1470	0.020	25.0	10.8	124.5	1.3
6	5.918	0.343	0.1518	0.049	32.5	10.1	121.6	1.2
7	6.057	0.212	0.1546	0.110	40.2	6.2	124.4	1.2
8	5.885	0.273	0.1561	0.174	46.2	8.0	120.9	1.4
9	5.953	0.209	0.1575	0.422	52.2	6.1	122.3	0.8
10	5.785	0.183	0.1634	1.231	58.9	5.4	119.0	1.1
11	5.930	0.166	0.1603	0.789	68.5	4.9	121.8	1.2
12	5.980	0.198	0.1574	0.127	73.8	5.8	122.8	1.2
13	5.835	0.189	0.1617	0.101	79.3	5.6	119.9	2.3
14	5.856	0.273	0.1569	0.159	83.5	8.0	120.4	1.3
15	5.452	0.248	0.1699	0.280	87.1	7.3	112.3	2.8
16	5.955	0.251	0.1553	0.672	91.6	7.4	122.3	0.6
17	6.015	0.084	0.1621	0.579	95.1	2.4	123.5	1.3
18	5.997	0.192	0.1571	0.951	96.9	5.6	123.2	2.5
19	6.144	0.012	0.1621	1.767	98.3	0.3	126.1	3.0
20	5.528	0.803	0.1379	3.159	100.0	23.7	113.8	3.7
						Total age = 120.9 ± 1.2		
LN110 biotite		*J = 0.011781*						
1	3.891	3.049	0.025	0.105	0.3	90.0	80.9	20.3
2	5.060	2.185	0.070	0.006	3.0	64.5	104.5	3.8
3	5.695	0.477	0.151	0.022	6.9	14.1	117.2	1.3
4	5.618	0.203	0.167	0.006	11.2	6.0	115.6	1.2
5	5.894	0.012	0.169	–	15.5	0.3	121.1	1.1
6	5.762	0.060	0.170	0.011	20.2	1.7	118.5	0.8
7	5.688	0.040	0.174	0.011	24.3	1.2	117.0	1.1
8	5.769	0.090	0.173	0.006	28.1	0.2	118.6	0.9
9	5.900	0.050	0.167	0.014	31.0	1.4	121.2	1.4
10	5.815	0.093	0.167	0.005	34.0	2.7	119.6	2.0
11	5.802	0.088	0.168	0.018	37.7	2.6	119.3	1.3
12	5.679	0.071	0.172	–	41.3	2.1	116.9	1.2
13	5.671	0.080	0.172	0.011	45.0	2.6	116.7	1.5
14	5.625	0.058	0.175	0.011	49.4	1.7	115.8	1.7
15	5.644	0.085	0.173	0.017	53.4	2.5	116.2	0.8
16	5.887	0.013	0.169	0.003	57.7	0.4	121.0	1.3
17	5.568	0.077	0.175	0.016	61.5	2.2	114.6	3.3
18	5.861	0.068	0.167	0.012	66.0	2.0	120.5	1.7
19	5.817	0.037	0.170	0.017	69.9	1.1	119.6	1.1
20	5.809	0.037	0.170	0.029	74.2	1.1	119.4	1.3
21	5.867	0.041	0.168	0.021	78.7	1.2	120.6	0.7
22	5.807	0.048	0.170	0.048	82.2	1.4	119.4	1.2
23	5.982	0.025	0.166	0.011	85.2	0.7	122.9	1.2
24	5.891	0.021	0.169	0.004	88.4	0.6	121.1	0.9
25	5.835	0.080	0.167	0.030	92.9	2.3	120.0	0.9
26	5.510	0.171	0.172	0.062	94.0	5.0	113.5	3.6
27	5.630	0.103	0.172	0.064	95.2	3.0	115.9	2.6
28	5.956	0.017	0.167	0.024	96.9	0.5	122.4	2.5
29	5.625	0.047	0.175	0.074	99.9	1.3	115.8	1.3
						Total age = 118.0 ± 1.		

pseudo-plateau ages range from 116.9 ± 1.4 Ma to 124.1 ± 1.3 Ma and the corresponding intercept ages between 118.1 ± 1.3 Ma to 124.9 ± 1.2 Ma (one sigma error). Cooling ages from mylonitized rocks do not reveal significant age differences between the southern and northern limbs of the dome and they agree with the biotite cooling age of an undeformed granite inside the dome also (sample LN110).

Four amphibole age spectra are shown in Fig. 4f–I, together with Ca/K spectra and reverse isochron plots in Fig. 4f′–I′. Two types of profile can be observed, depending on the nature of the protolith. For mylonitic granodiorite (LN83) and gneissic migmatite (LN85), the age spectra are partially discordant and yield pseudo-plateau ages respectively of 121.7 ± 1.6 and 116.4 ± 1.5 Ma, being in agreement with the biotite dates. In the $^{36}Ar/^{40}Ar$ vs. $^{39}Ar/^{40}Ar$ correlation plot, sample LN85 has an intercept age similar to the pseudo-plateau. By contrast, sample LN83 has an intercept age that is by 4 Ma younger than its pseudo-plateau age, and its initial argon ratio above 295.5 suggests the presence of a minor amount of excess argon. The age spectra from two amphibolites (Fig. 4f and g) are strongly discordant and characterized by a bump in the middle portion of the spectrum; no correlation with Ca/K variations can be observed. During step heating, apparent ages increase from minimum values in the range 100–130 Ma to maxima of 255 Ma for LN 59 and 331 Ma for LN 70. Then, ages decrease to values that range from 150 to 280 Ma. No intercept age can be defined for these two amphiboles in the reverse isochron plot.

3.2. U–Pb dating

A granodioritic intrusion (LN 82) occurring close to the detachment zone in the western side of the massif was collected to date primary magmatic titanite that crystallized from the granitic melt. The euhedral grains vary in size from a few micro-meters to about 0.4 mm, with a mean length of about 0.2 mm. In pleochroism, the transparent grains range from honey-brown to yellow carrying in some cases opaque inclusions, typical of titanites from rocks formed by crustal melting (Schärer and Labrousse, 2003). After

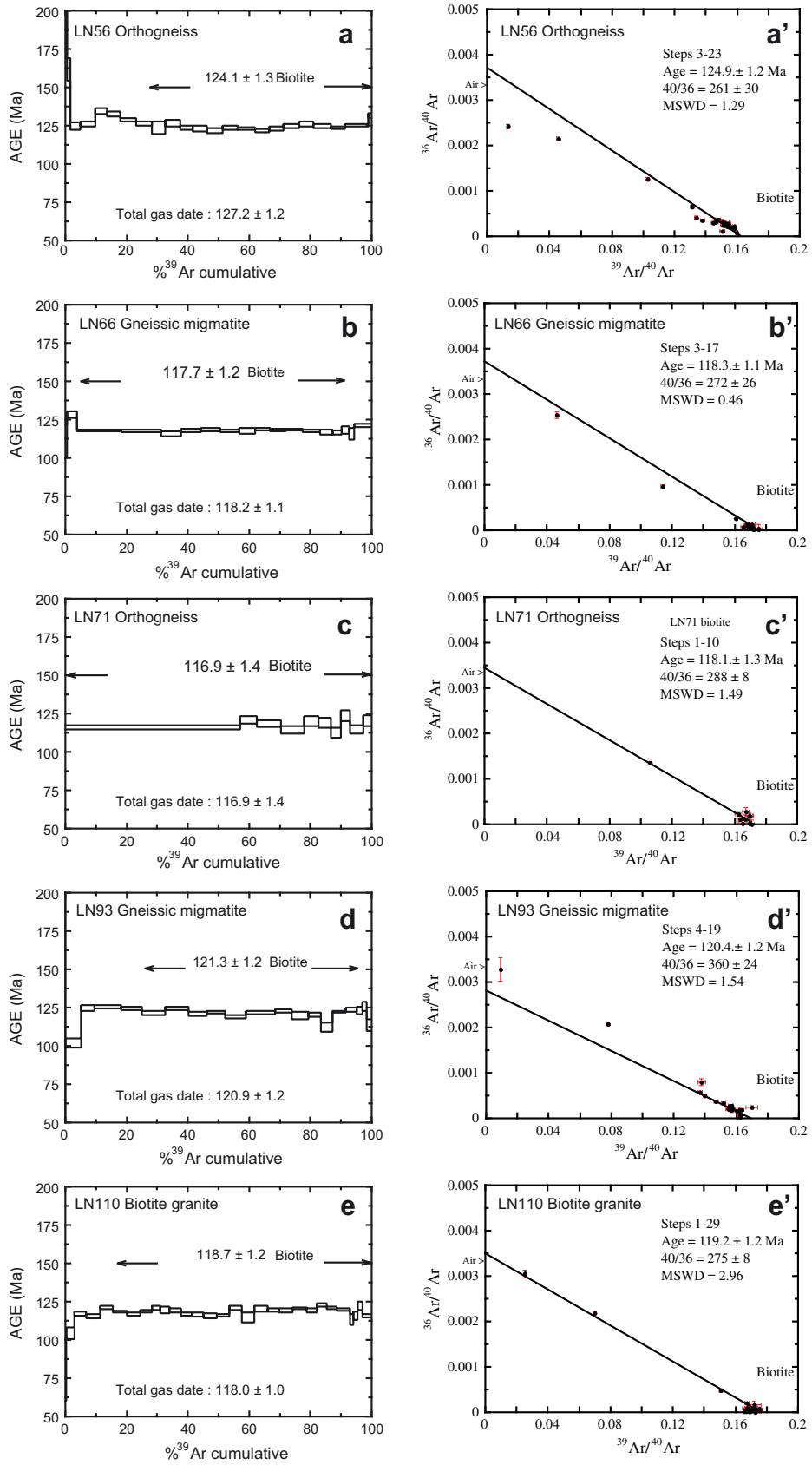

Fig. 4. $^{40}Ar/^{39}Ar$ age spectra (a–e) and reverse isochron plots (a′–e′) of biotite, amphibole (f–i) and reverse isochron plots (f′–i′), from gneissic migmatites, amphibolite, orthogneiss, mylonitic, and undeformed granite from south-Liaodong peninsula massif. Ca/K plots are shown for amphiboles. They are derived from the $^{37}Ar/^{39}Ar$ ratios measured at each step and provide information on the chemical homogeneity or heterogeneity of the dated mineral such as compositional zoning, or contamination by inclusions.

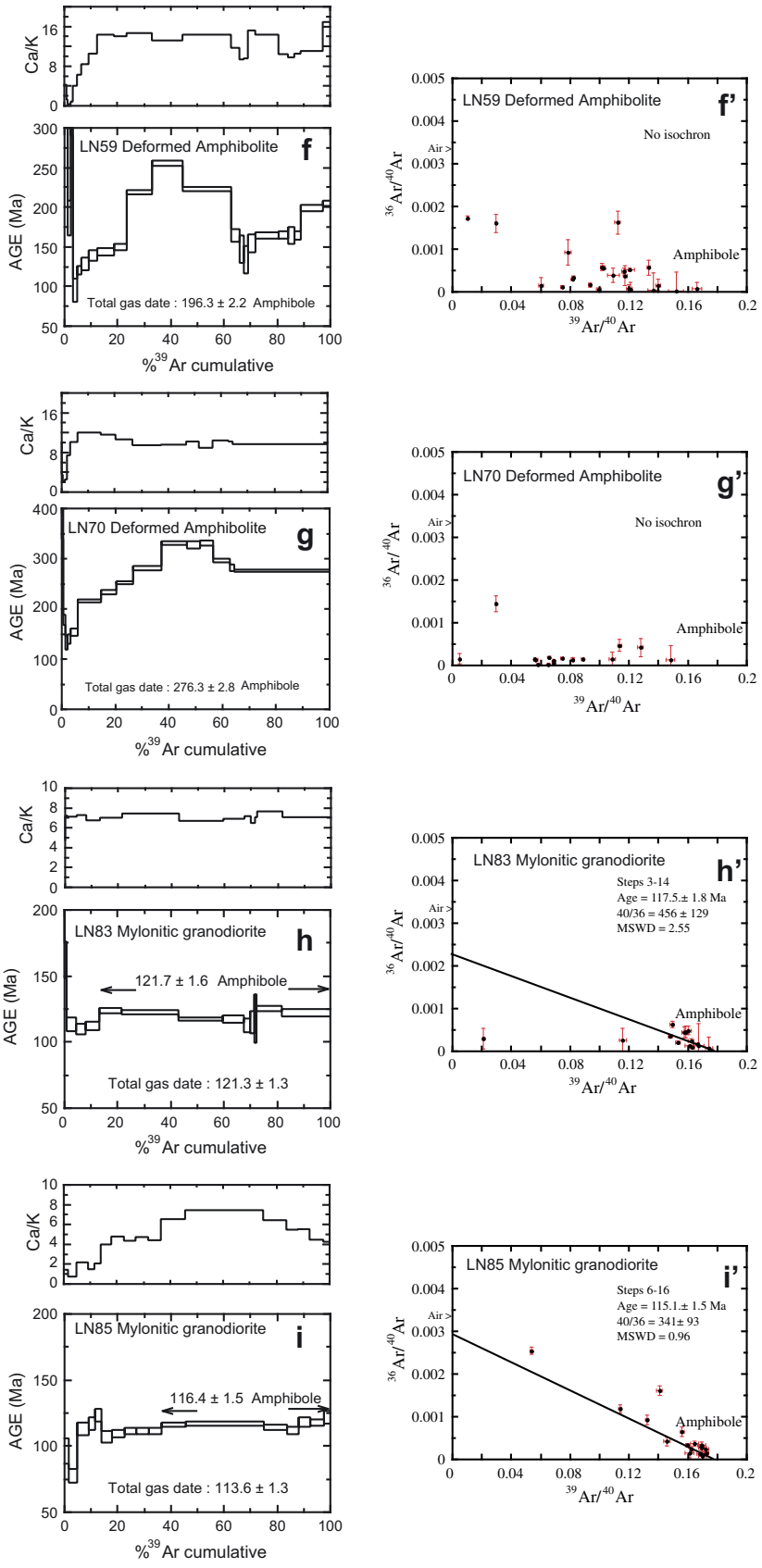

Fig. 4 (*continued*)

mechanical abrasion of some grains with pyrite (Table 3; Krogh, 1982), the 4 N HNO_3-washed titanites were individually selected to constitute size-fractions representative of the entire population. Seven such fractions were analyzed for U–Pb (Table 3), as well as

Table 3
U–Pb analytical results for titanite size-fractions, and initial Pb isotopic composition of cogenetic K-feldspar.

Sample description (see also footnotes)	Wt (mg)	Concentrations (ppm)		$^{206}Pb/^{204}Pb$ measured[b]	Radiogenic Pb[c] (atomic %)			Atomic ratios[c]		Apparent ages (Ma)	
		U	Pbrad		^{206}Pb	^{207}Pb	^{208}Pb	$^{206}Pb/^{238}U$	$^{207}Pb/^{235}U$	$^{206}Pb/^{238}U$	$^{207}Pb/^{235}U$
Leucosome layer LN-82 (N 39°21.93′ ; E 121°55.63′) Titanite[a]											
(1) 5 large gr., op. incl., not abr.	0.267	133	3.46	124.5	82.9	3.8	13.3	0.02508	0.1579	159.7	148.8
(2) 3 large gr, op. incl., not abr.	0.343	127	3.33	98.1	81.8	3.9	14.3	0.02486	0.1626	158.3	153.0
(3) 8 medium-size gr., op. incl., not abr.	0.219	141	3.33	101.5	81.4	3.7	14.9	0.02230	0.1407	142.2	133.7
(4) 9 medium-size gr., abr.	0.248	119	3.17	127.7	82.6	3.7	13.7	0.02551	0.1594	162.4	150.2
(5) 5 large gr., abr	0.304	137	3.45	121.2	81.2	3.6	15.2	0.02536	0.1568	161.5	147.9
(6) 13 small gr., abr	0.227	129	3.42	122.5	85.0	3.7	11.3	0.02483	0.1499	158.1	141.8
(7) 4 large gr., op. incl., abr.	0.240	119	3.69	129.8	82.7	3.7	13.6	0.02548	0.1577	162.2	148.7
(8) K-fsp (10 mg of 300–500 μm gr.) $^{206}Pb/^{204}Pb$: 17.810 ± 0.027; $^{207}Pb/^{204}Pb$: 15.718 ± 0.021; $^{208}Pb/^{204}Pb$: 38.481 ± 0.060[d]											

[a] number of grains; medium-size gr: small grains (gr.) <100 μm; medium-size gr. 100–150 μm; large gr. >150 μm; *op*: opaque Inc.: inclusion; *abr*: abraded. Prior to mechanical abrasion with pyrite (Krogh, 1982) most grains were euhedral, including some fragments of larger grains.
[b] Ratio corrected for mass-discrimination (0.10 ± 0.05%/amu) and isotopic tracer contribution.
[c] Corrected for mass-discrimination, isotopic tracer contribution, 60 pg of Pb blank, 1 pg of U blank, and initial common lead (see [d]).
[d] Initial common Pb measured in cogenetic K-fsp., corrected for mass discrimination (Pb blank is negligible).

cogenetic K-feldspar to determine initial Pb isotopic composition at the time of melt crystallization. The 0.22–0.34 mg fractions carry between 119 and 141 ppm of U, and corresponding radiogenic Pb lies between 3.17 and 3.69 ppm. In the Concordia plot, (Fig. 5) six of the analyses yield ages that are identical within analytical uncertainty (ellipses), lying slightly to the left of the Concordia curve. One fraction yields younger ages. Although the deviation of the five fractions from the curve is only of the order of 1%, it is analytically significant, whereas one analysis lies on the curve, with one having identical ages to the other grain fractions. To explain such a deviation, the following three possibilities have to be considered: (1) isotopic compositions of common Pb in K-feldspar are varying, being identical to Pb initial compositions only in some of the titanites (the concordant data), (2) the grains are affected by minor relative U-loss, and (3) deviation is due to initial disequilibrium, relative to initial excess of ^{230}Th in the ^{238}U decay chain (Schärer, 1984). To examine hypothesis (1), we have calculated the ages with model Pb isotopic compositions for upper (Zartman and Doe, 1981) and average (Stacey and Kramers, 1975) Phanerozoic and Precambrian continental crust but none of the compositions brings the individual dates on the Concordia curve. Hypothesis (2) cannot completely be ruled out; however, it is not very likely since re-opening of the U–Pb clock would result in a spread of data along their $^{207}Pb/^{206}Pb$ slope; there is very little chance to have identical ages for 6 of 7 analyses and in particular, if one considers that both abraded and not abraded grains define the identical ages. Point (3), (excess ^{206}Pb from initial excess in ^{230}Th) is not likely because Th/U in this mineral is not high enough to cause measurable disequilibrium after more than 150 m.y. of radioactive decay (calculated from radiogenic ^{208}Pb, Table 3). However, if very recent slight titanite overgrowth has occurred it could potentially induce disequilibrium on the order of 1%, but in this case, abraded and non-abraded grains would not give the same age. Thus this possibility appears as unlikely.

Since the dominant uncertainty lies in ^{207}Pb, which is very sensitive to any change in initial Pb compositions, the mean value of $^{206}Pb/^{238}U$ ratios (6 fractions with identical ages) was chosen to derive the age of 160.4 ± 1.4 (2 sigma) Ma for titanite crystallization in the granodiorite. If alternatively, both $^{206}Pb/^{238}U$ and $^{207}Pb/^{235}U$ are used for calculation (including the entire extent of potential perturbation) a mean age of 154.4 ± 5.4 Ma is obtained, being within analytical error identical with the $^{206}Pb/^{238}U$ mean age.

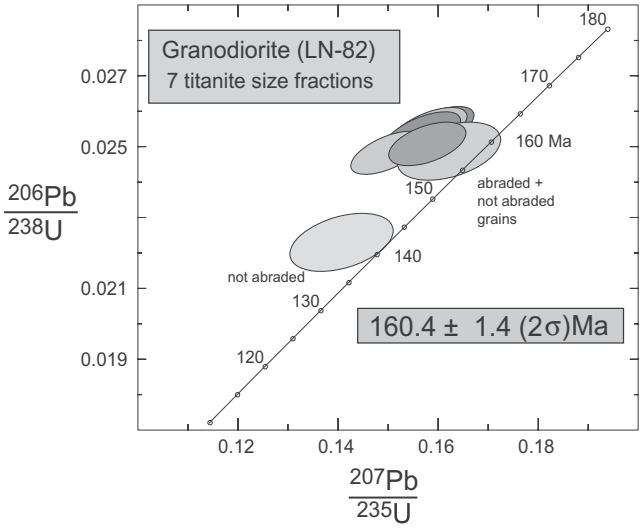

Fig. 5. U/Pb concordia diagram of titanite fractions from the granodiorite (sample LN 82). See Table 3 for analytical data.

3.3. Age interpretations

In spite of the unexplained slight deviation of about 1% from the Concordia curve, the U–Pb ages unambiguously document granodiorite emplacement around 160 Ma, i.e. in Middle Jurassic (Dogger) times. Since the U–Pb chronometer behaves as a closed system above 630 °C (Zhang and Schärer, 1996) this age can be considered to reflect the time of crystallization of the granodioritic magma within the rather cool country gneisses. In the study area, Middle Jurassic ages are also found for three granodioritic plutons that crop out immediately near the one dated here (Wu et al., 2005b; Fig. 3). On the other hand, monzogranitic plutons intruding the south-Liaodong peninsula MCC yield Early Cretaceous U/Pb ages ranging from 130 to 120 Ma (Wu et al., 2005a; Fig. 3). The tectonic setting of this magmatism will be discussed in the next section.

Subsequent tectono-metamorphic events led to the deformation of the Jurassic granites, with $^{40}Ar/^{39}Ar$ dating of amphibole and biotite giving ages of 124–110 Ma that, according to available geochronological data, are coeval with the emplacement of a second generation of early to mid-Cretaceous granitoids. Given the difference in closure temperature for the dated minerals (≈300 °C for biotite and ≈550 °C for amphibole, Harrison et al., 1985; Dahl, 1996), the concordance of $^{40}Ar/^{39}Ar$ ages indicates

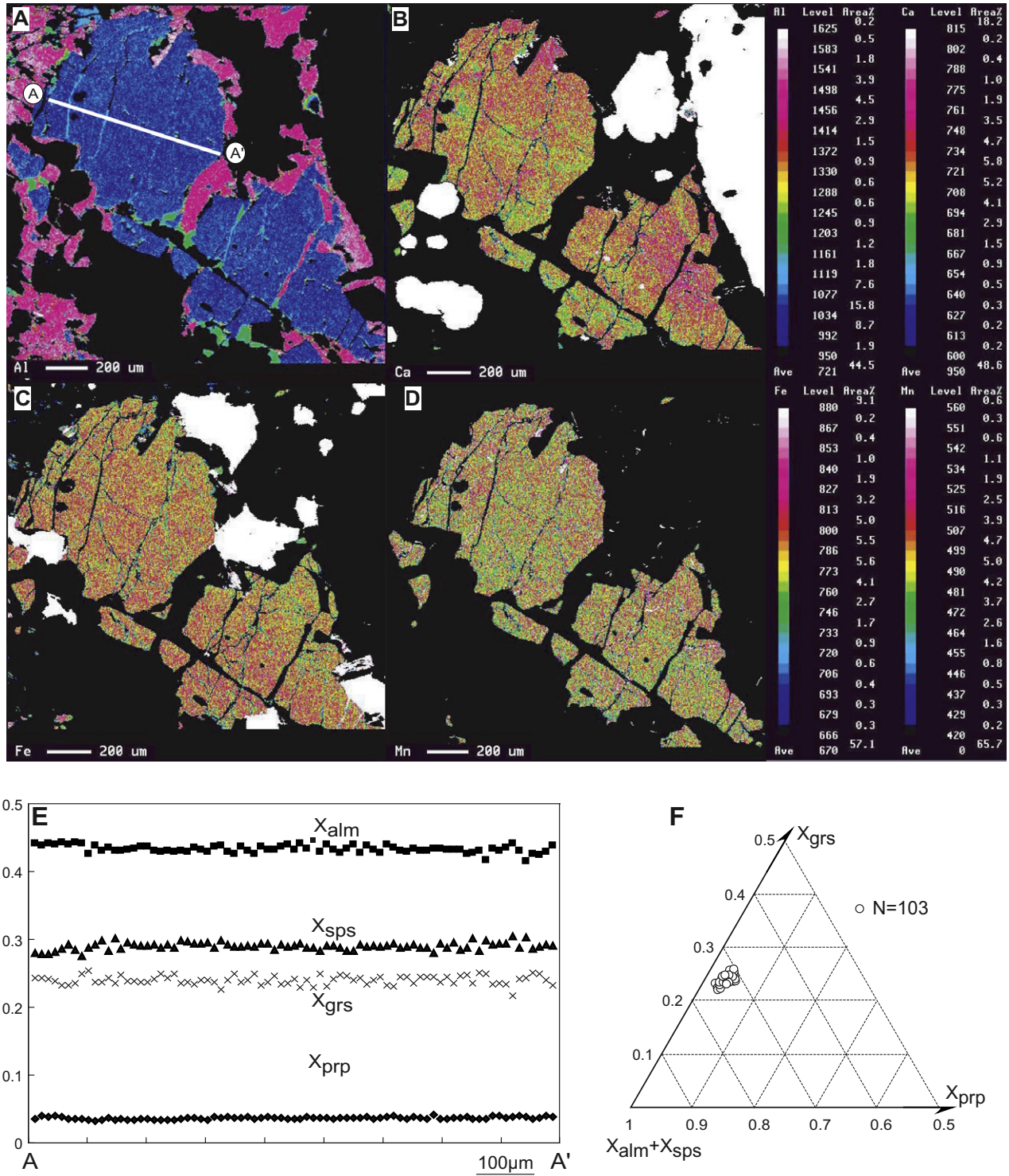

Fig. 6. Chemical analysis of magmatic anhedral garnet in the ductilely sheared Jurassic granodiorite (sample LN 84). (A): Al Kα, (B): Ca Kα, (C): Fe Kα (D): Mn Kα X-ray mapping images. Warm color indicates high concentration of element. (E): step-scanning analyses along the A–A′ profile. (F): chemical composition. Abbreviations of end-members are: alm: almandine; sps: spessartine; prp: pyrope; grs: grossular.

relatively fast cooling of mylonitized gneisses and granodiorites from the detachment zone, as well as the undeformed granites below. In this context, it is suggested that fast cooling was triggered by partial removal of the hanging-wall rocks leading to the rapid exhumation of the footwall rocks during extensional tectonics, promoting fast ascent of isotherms to upper crustal levels. Structures observed in the Cretaceous monzogranitic pluton in the footwall are compatible with the idea that the NW-directed movements were coeval with the generation of deep crustal melts that migrated to upper levels as denudation was progressing (Lin et al., 2008b).

Two amphiboles from the south-Liaodong peninsula MCC yield strongly different age spectra having total gas ages around 200 and 280 Ma, respectively (samples LN 59 and LN 70; Fig. 4f and g).

Table 4
Representative compositions for garnet, hastigsite, biotite, plagioclase and epidote.

Minerals	Garnet		Hastigsite		Biotite		Plagioclase		Epidote
Position	Rim	Core	Rim	Core	Rim	Core	Rim	Core	Matrix
SiO_2	37.15	37.21	40.71	40.31	35.74	36.04	61.12	60.08	37.91
TiO_2	0.09	0.14	0.79	0.95	2.76	2.69	0.04	0.00	23.92
Al_2O_3	19.89	19.71	11.12	12.54	14.65	14.69	24.90	24.72	0.00
FeO	17.90	18.22	19.03	21.07	17.98	17.67	0.10	0.06	11.68
Cr_2O_3	0.01	0.01	0.00	0.04	0.00	0.00	0.00	0.00	0.00
MnO	11.93	11.97	1.24	1.15	1.01	0.99	0.00	0.00	0.00
MgO	0.79	0.82	7.66	6.88	11.21	11.52	0.00	0.02	0.02
CaO	11.86	11.87	11.68	11.50	0.59	0.50	5.82	6.08	23.47
Na_2O	0.00	0.29	1.76	1.43	0.09	0.11	8.49	7.53	0.00
K_2O	0.00	0.00	1.41	1.53	5.89	6.09	0.20	0.83	0.00
Total	99.62	100.23	95.38	97.41	89.92	90.31	100.66	99.32	97.00
O	12	12	23	23	11	11	8	8	12.5
Si	2.98	2.97	6.39	6.19	2.84	2.84	2.70	2.70	3.00
Al^{IV}	0.02	0.04	1.61	1.81	0.16	0.16	1.30	1.31	2.23
Al^{VI}	1.87	1.81	0.45	0.46	1.21	1.21	0.00	0.00	0.00
Cr	0.00	0.00	0.00	0.01	0.00	0.00	0.00	0.00	0.00
Fe^{3+}	0.13	0.24	0.22	0.62	0.00	0.00	0.00	0.00	0.77
Ti	0.01	0.01	0.09	0.11	0.17	0.16	0.00	0.00	0.00
Fe^{2+}	1.07	0.97	2.28	2.08	1.19	1.17	0.00	0.00	0.00
Mg	0.10	0.10	1.79	1.58	1.33	1.36	0.00	0.00	0.00
Mn	0.81	0.81	0.16	0.15	0.07	0.07	0.00	0.00	0.00
Ca	1.02	1.01	1.97	1.89	0.05	0.04	0.28	0.29	1.99
Na	0.00	0.05	0.54	0.43	0.01	0.02	0.73	0.66	0.00
K	0.00	0.00	0.28	0.30	0.60	0.61	0.01	0.05	0.00
Sum	8.00	8.00	15.78	15.62	7.62	7.63	5.02	5.00	8.00

Since the dated rocks are amphibolite boudins within Archean gneisses, it is very likely that inherited argon causes the observed age scatter. Such in excess Ar was probably not totally been released from the boudins during Cretaceous heating of the Archean basement, due to the fact that these boudins were less affected by deformation and recrystallization than their host gneiss. Several biotites also display evidence for a minor contamination by excess argon, released during the first heating increments. It is very likely that such excess argon in biotite was trapped on the grain surface and along its lattice defects, related to late fluid circulation and weathering.

4. Metamorphism and microstructure of the granodiorite involved in syn-exhumational metamorphism

In the south-Liaodong peninsula MCC, the Jurassic granodioritic plutons were affected by the ductile detachment fault, and experienced metamorphism and deformation during their exhumation. Petrological analysis will allow us to understand the metamorphism and deformation history of this orthogneiss. Combined with $^{40}Ar/^{39}Ar$ and U/Pb geochronological results (cf. Section 3), the *P–T–t* path of the south-Liaodong peninsula MCC can be established.

Sample LN 84 is a foliated Jurassic granodiorite (located in the same outcrop than sample LN 85, Fig. 3), which contains quartz, plagioclase and biotite as major phases, and garnet, calcic-amphibole (hastingsite), albite, and titanite as minor ones. Moreover, some minerals (for instance epidote, albite, chlorite, and pyrite) are secondary metamorphic ones crystallized during the ductile shearing. Chemical analyses of garnet, amphibole, epidote, and allanite are provided below. Anhedral garnet with no inclusions is surrounded by oligoclase (Fig. 6A–D). This texture shows that oligoclase crystallized at a relatively late stage. Calcic amphibole with euhedral or subhedral habit is oriented along the shear bands and presents an asymmetric shape consistent with the regional kinematic pattern. Chlorite distributed around amphibole indicates that it developed under retrogressive greenschist facies conditions during the late stage of deformation.

Quantitative analyses and X-ray mapping were carried out using a JEOL JXA-8800R electron-probe microanalyzer (EPMA) with WDS (Wave-dispersive-spectrometer) and EDS (Energy-dispersive-spectrometer) systems at the Petrological Laboratory of Nagoya University. Accelerating voltage, specimen current and beam diameter for quantitative analyses were 15 kV, 12 nA on the Faraday cup and 2–3 μm, respectively. Well-characterized natural and synthetic phases were used as standards. The ZAF was employed for matrix correction. Amphibole nomenclature follows Leake et al. (1997) and Fe^{3+}/Fe^{2+} values were calculated with total cations number of 13, excluding Ca, Ba, Na and K (O = 23). For garnet, all iron was assumed to be ferrous and its end-member proportion (X_i) was calculated as $i/(Fe + Mn + Mg + Ca)$.

4.1. Garnet

Garnet belongs to the Mg-poor (less than 1 wt.% MgO) and Mn and Ca-rich (up to12 wt.% CaO) almandine-spessartite series (Fig. 6F and Table 4). X-ray mapping and quantitative analysis results show the garnet is almost homogeneous (Fig. 6E). X (mole fraction) in garnet is 0.32–0.37 for X_{Fe} [$=Fe^{2+}/(Ca + Mg + Fe^{2+} + Mn)$], 0.33–0.36 for X_{Ca} [$=Ca/(Ca + Mg + Fe^{2+} + Mn)$], 0.26–0.29 of X_{Mn} [$=Mn/(Mn + Mg + Fe^{2+} + Mn)$] and 0.03–0.04 of X_{Mg} [$=Mg/(Ca + Mg + Fe^{2+} + Mn)$], respectively (Fig. 6F and Table 4).

4.2. Amphibole

Amphiboles form several millimeter-sized grains, and most of them are hastingsite with Si = 6.16–6.42 per formula unit (pfu), $^{[B]}Na$ = 0.03–0.20 pfu and $^{[A]}(Na + K)$ = 0.33–0.86 pfu (Fig. 7A and Table 4). TiO_2 and K_2O contents are less than 1.1 wt.% and 1.9 wt.%, respectively (Table 4). Due to late metamorphic re-equilibrium, hastingsite develops a retrogressive zonation with Al^{3+}

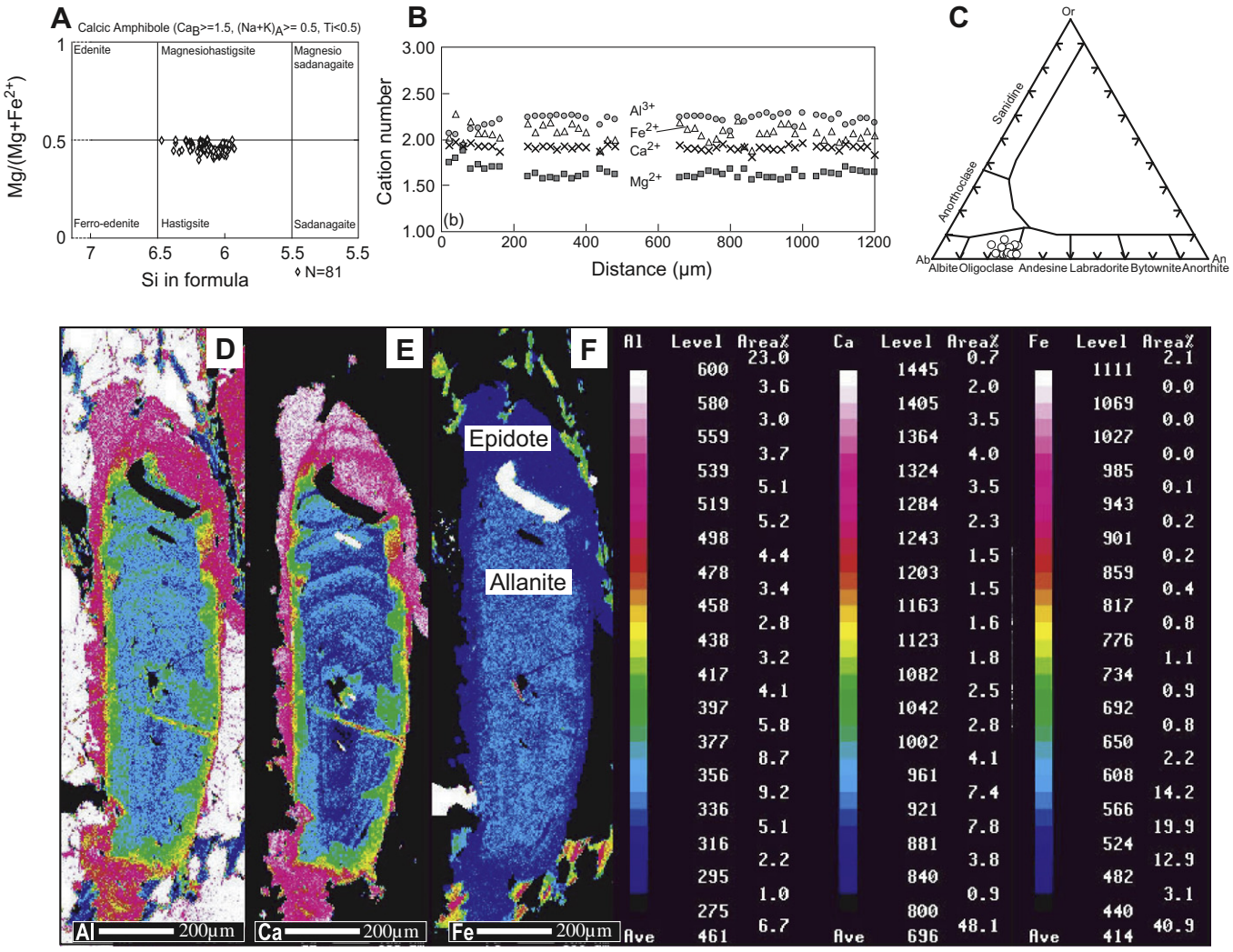

Fig. 7. Chemical compositions of amphibole, feldspar, epidote, and allanite from the Jurassic granodiorite (sample LN 84). (A) Leake et al. (1997) plot showing that the analyzed amphibole is hastingsite. (B) Elemental chemical composition profiles for Al^{3+}, Fe^{2+}, Ca^{2+}, Mg^{2+} of amphibole from the Jurassic granodiorite showing the absence of zoning. (C) Chemical composition of feldspar in the Jurassic granodiorite indicating an oligoclase composition. Abbreviations of end-members are: Ab: Albite; An: Anorthite; Or: Orthoclase. (D) Al Kα, (E) Ca Kα and (F) Fe Kα X-ray mapping images of anhedral magmatic allanite rimmed by metamorphic epidote. Warm and bright colors indicate high element concentration.

pfu decreasing from 2.29 to 1.94 from core to rim (Fig. 7B). This could be indicative of a pressure decrease.

4.3. Other minerals

Most of analyzed plagioclase consists of 65–75% albite, 22–30% anorthite and 0.9–5% K-feldspar (Fig. 7C and Table 4). X_{Fe} [=Fe^{3+}/(Fe^{3+}+Al + Cr) as total Fe as Fe^{3+}] of epidote is around 0.30; FeO and MgO for biotite are 16.94–18.66 wt.% and 10.26–11.85 wt.%. These minerals have no clear zoning in the grains of the matrix (Table 4).

4.4. P–T emplacement conditions of the Jurassic granodiorite

South of Pulandian city, a mylonitized garnet-bearing granodiorite yields a titanite U/Pb age of 160.4 ± 1.4 Ma (cf. above Section 3), while calcic magmatic amphibole has a $^{40}Ar/^{39}Ar$ age of 121.7 ± 1.6 Ma. According to the isotopic closure temperature of these minerals, we can infer that the former date represents the crystallization age of the magmatic protolith and the latter corresponds to its time of cooling to 550 °C. Because this age is concordant with synkinematic biotite cooling ages, it is likely that ca.120 Ma also dates the mylonitic event responsible for the final exhumation of the granodiorite.

Allanite is an important accessory mineral in granitic rocks, but has been less investigated in the metamorphic rocks. In our sample (LN84 which is similar to sample LN 85, Fig. 3) allanite is abundant. It shows a relatively large compositional range and a complex zonal structure as revealed by X-ray mapping (Fig. 7D–F). The zonation of the epidote minerals argues for two quite different stages of crystallization. The Fe rich and Al, Ca poor rhythmic clitellums of the core developed during magmatic crystallization (Jiang et al., 2003). It is more difficult to decide if the rim of epidote crystallized during the magmatic or metamorphism stage. According to our knowledge of the regional geology, it is likely that the epidote rim formed during the epidote–amphibolite to greenschist facies solid state metamorphism that overprinted the magmatic assemblage.

In order to determine the peak *P–T* conditions for the garnet-bearing gneisses, Grt-Amp-Pl (Kohn and Spear, 1990), Grt-Bt-Pl-Qtz (Wu et al., 2004), the amphibole aluminum geobarometer (Hammarstrom and Zen, 1986; Hollister et al., 1987; Johnson

et al., 1989; Schmidt, 1992), Grt-Amp (Krogh-Ravna, 2000), and Grt-Bt (Holdaway, 2000) thermometers were used. Mineral compositions of garnet core, amphibole, biotite and plagioclase have been used as they have not been disturbed by the later metamorphism as shown by the above study of their composition profiles (Figs. 6E, 7A and B). 16 mineral pairs were selected to derive estimates of peak *P–T* conditions and these are listed in Table 5.

P–T estimates using the Kohn and Spear (1990) barometer and Krogh-Ravna (2000) thermometer (first two columns in Table 5) are 0.95–1.09 GPa ($\bar{x} = 1.01$, $1\sigma = 0.04$ GPa) and 585–696 °C ($\bar{x} = 651$°C, $1\sigma = 31$ °C). Estimates using the Wu et al. (2004) barometer and Holdaway (2000) thermometer are 0.81–097 GPa ($\bar{x} = 0.87$, $1\sigma = 0.04$GPa) and 556–582 °C ($\bar{x} = 569$°C, $1\sigma = 8$ °C). Considering the amphibole aluminum geobarometer is suitable for granitic rocks, very similar results are provided according to the different authors (Table 5; Hammarstrom and Zen, 1986; Hollister et al., 1987; Johnson et al., 1989; Schmidt, 1992). Usually, the pressure estimate given by Schmidt (1992) is considered the beat for mylonitic granodiorite (Ratschbacher et al., 2000), and gives an average pressure of 0.74 ± 0.05 GPa (Table 5; Fig. 8). The thermobarometers of Holdaway (2000) and Wu et al. (2004) could potentially give more accurate *P–T* values, as the same activity models for garnet and biotite in the Grt-Bt thermometer (Holdaway, 2000) and Grt-Bt-Pl-Qtz barometer (Wu et al., 2004) are applied respectively, and the garnet, biotite and plagioclase seem not to have been influenced by later metamorphism. Hence, the peak *P–T* conditions calculated using the thermobarometers of Holdaway (2000) and Wu et al. (2004) may be close to 'peak' *P–T* conditions, and record an average *P–T* value of 569 ± 8 °C and 0.87 ± 0.04 GPa.

Assuming a rock density of 2800 kg/m^3 on average (Ratschbacher et al., 2000; Zheng, 1997), this Jurassic granitoids was emplaced around 26–31 km depth. This result is in agreement with the granite isotopic geochemistry, as a low $(^{87}Sr/^{86}Sr)_i$ ratio and a high εNd(t) value indicate that the Jurassic plutons originated from the partial melting of juvenile lower crust (Wu et al., 2005b). If this interpretation is correct, the temperature gradient in the Jurassic crust was about 20 °C/km. Such a value complies with the thermal gradient derived from vitrinite reflectance (Ro) of Mesozoic sedimentary rocks of North China and indicates that the research area had stable cratonic crust during the Jurassic to Early Cretaceous (Fu et al., 2005; Zhai et al., 2004).

Table 5
The peak *P–T* conditions for deformed garnet-bearing granodiorite.

Sample	P_{K90}	T_{K20}	P_{W04}	T_{H20}	P_{H86}	P_{H87}	P_{J89}	P_{S92}
1	1.09	696	0.92	577	0.74	0.79	0.90	0.77
2	1.06	675	0.91	576	0.74	0.79	0.90	0.77
3	1.03	676	0.87	568	0.74	0.80	0.91	0.77
4	1.00	668	0.82	564	0.74	0.80	0.91	0.77
5	1.03	680	0.84	569	0.75	0.80	0.91	0.78
6	1.00	641	0.81	556	0.74	0.80	0.91	0.77
7	1.01	659	0.83	561	0.75	0.80	0.91	0.78
8	1.02	667	0.85	565	0.74	0.80	0.91	0.77
9	0.98	627	0.82	558	0.73	0.78	0.90	0.76
10	0.98	637	0.88	571	0.69	0.74	0.87	0.72
11	1.02	658	0.86	572	0.73	0.79	0.90	0.76
12	1.07	685	0.85	579	0.72	0.78	0.89	0.76
13	0.97	608	0.85	564	0.71	0.76	0.88	0.74
14	0.95	585	0.89	568	0.63	0.67	0.81	0.66
15	1.00	630	0.97	582	0.57	0.60	0.76	0.61
16	0.96	618	0.92	575	0.61	0.64	0.79	0.64
Average	1.01	651	0.87	569	0.71	0.76	0.88	0.74
STDV	0.04	31	0.04	8	0.06	0.06	0.05	0.05

P_{K90}: the Grt-Amp-Pl barometer of Kohn and Spear (1990); T_{K20}: the Grt-Amp thermometer from Krogh-Ravna (2000); P_{W04}: the Grt-Bt-Pl-Qtz barometers of Wu et al. (2004); T_{H20}: the Grt-Bt themometer of Holdaway (2000); P_{H86}, P_{H87}, P_{J89} and P_{S92}: the amphibole aluminum geobarometer from Hammarstrom and Zen (1986), Hollister et al. (1987), Johnson et al. (1989) and Schmidt (1992), respectively.

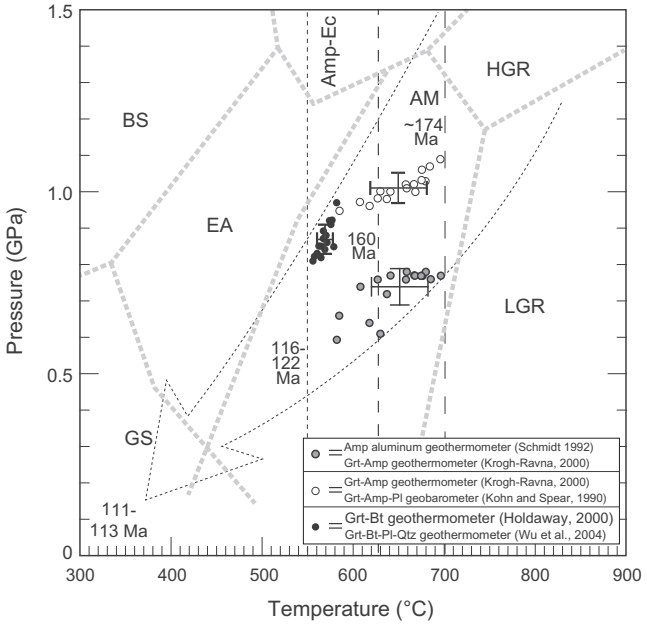

Fig. 8. *P–T* diagram showing the peak metamorphic conditions for the garnet-bearing Jurassic gneissic granodiorite of the south-Liaodong peninsula MCC, based on different thermobarometers. Metamorphic facies grid is from Okamoto and Maruyama (1999). (Black crosses show the average error). BS: Blueschist; EA: Epidote–amphibolite; GS: Greenschist; AM: Amphibolite; Amp-Ec, Amphibolite-eclogite; HGR: High temperature granulite; LGR: Low temperature granulite.

5. Discussion

5.1. A two phase cooling history for the south-Liaodong peninsula MCC

The Jurassic granodiorite and Cretaceous monzogranite show very different cooling histories (Fig. 9). This suggests that the granitic and metamorphic rocks in the south-Liaodong peninsula MCC experienced two distinct exhumation stages. South of Pulandian city, in the footwall of the detachment fault, zircon and titanite from granodiorite yield U/Pb ages of 170–177 Ma and 160 Ma, respectively (Wu et al., 2005b; Yang et al., 2007a; Fig. 3). The hornblende $^{40}Ar/^{39}Ar$ ages of 121.7–116 Ma obtained from the mylonitized granodiorite allow us to derive a cooling rate of about 3 °C/my from zircon crystallization temperatures of ca. 700–800 °C, passing the titanite crystallization temperatures of ca. 630 °C, to hornblende closure temperature of ca. 550 °C (Fig. 9). In contrast, the Cretaceous monzogranite records U/Pb zircon ages around 128–118 Ma (Wu et al., 2005a), biotite and K-feldspar $^{40}Ar/^{39}Ar$ ages obtained from the pluton are 113–111 Ma and 118–112 Ma, respectively (Fig. 3; Yang et al., 2007b). When combined with amphibole ages of the Jurassic granodiorite (Fig. 9), the cooling rate is about 40–55 °C/my (Fig. 9). This result showing a fast cooling rate for the south Liaodong MCC is in agreement with previous work on metamorphic core complexes and syn-tectonic granites reported in Eastern China (Ratschbacher et al., 2000; Yang et al., 2004, 2007b, 2008; Wang and Li, 2008). Because of the lack of minerals with a closure temperature between titanite and amphibole (i.e. 630–550 °C), we cannot precisely estimate the cooling and exhumation history during the 160–122 Ma interval. Four possibilities are suggested here:

(1) *Slow continuous cooling*. Considering the zircon and titanite U/Pb, and the hornblende $^{40}Ar/^{39}Ar$ ages, a slow cooling rate of about 3 °C/my can be derived. Such a slow cooling path means that during ca. 40 My, from 160 Ma to 122 Ma, the

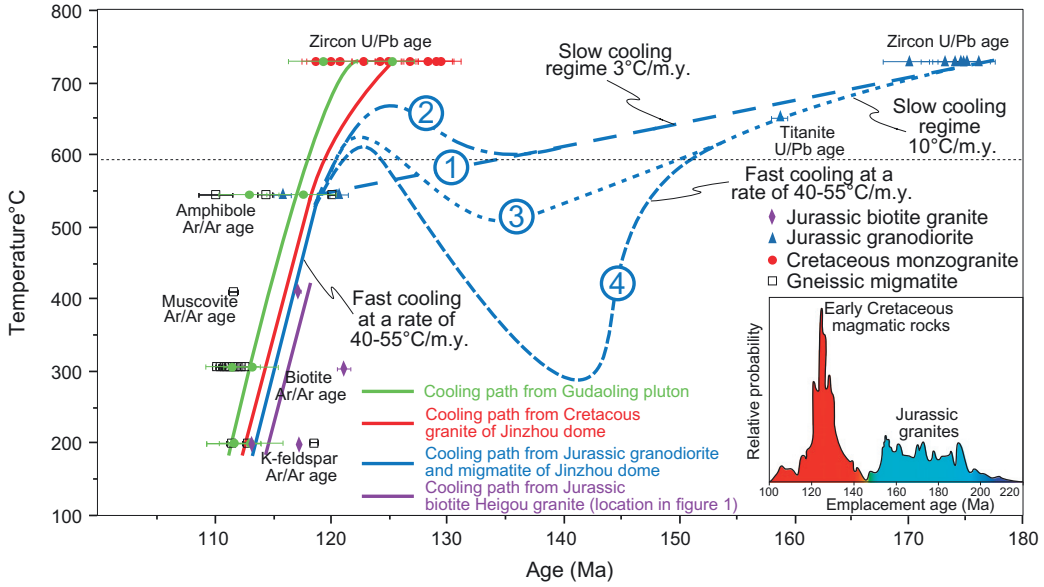

Fig. 9. Possible cooling paths of the south-Liaodong peninsula massif. Continuous lines corresponds to the Cretaceous cooling after 550 °C, different dashed lines indicate the different possibilities for the cooling history of the deformed Jurassic pluton. Path 1 corresponds to a slow cooling rate (3 °C/my) followed by a fast cooling (40–55 °C/my). Path 2 corresponds to an Early Cretaceous thermal pulse overprinting cooled Jurassic plutons. Path 3 corresponds to a slow cooling rate (10 °C/my) and progressive reheating by an Early Cretaceous thermal pulse overprinting the Jurassic cooling trend. Path 4 corresponds to two pulses of syn-kinematic plutonism. In this case, the Late Jurassic granodiorite experienced a fast cooling rate after its emplacement. In Early Cretaceous time, the new plutonic pulse reheated the already cooled Jurassic pluton and its country rocks. Inset shows the age distribution of the Mesozoic igneous rocks in eastern China and North Korea (n = 393). Two important periods of magmatism are identified, namely a Cretaceous event at ca. 125 Ma and a Jurassic one between 195 Ma to 155 Ma (from Davis et al., 2001; Cheng et al., 2006; Yang et al., 2004, 2006, 2008; Wu et al., 2005a,b, 2006, 2007).

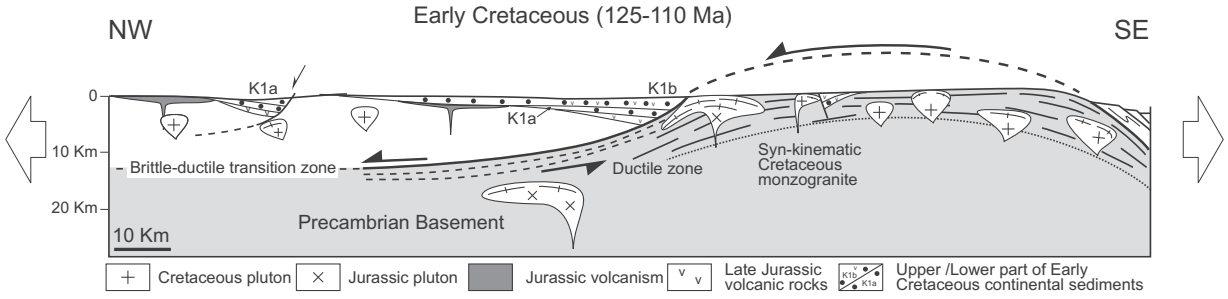

Fig. 10. Schematic tectonic sketch depicting the crustal deformation of the south-Liaodong Peninsula area during the Early Cretaceous. At this time, the crust experienced extensional tectonics represented by the formation of an asymmetric metamorphic core complex, ductile shearing of already emplaced Jurassic granodioritic plutons, emplacement of undeformed Cretaceous plutons, and sedimentary infill of half-grabens.

crust of the Liaodong peninsula area remained rather stable and thermally undisturbed until the emplacement of the Cretaceous plutons.

(2) *Slow cooling and Cretaceous reheating*. As in other places in the eastern part of the NCC, the Early Cretaceous is a period of intense plutonism during which the crust reached a high temperature (Zhai et al., 2004). This heating event would have influenced the cooling history of the Jurassic plutons. Such a reheating effect during the Early Cretaceous is shown in the cooling path (2) drawn on Fig. 9. A similar thermal overprint has been reported in the eastern part of the Qinling Belt, in Dabieshan and Lushan areas (Faure et al., 2003a; Lin et al., 2000). This suggests that the Cretaceous thermal event was a widespread phenomenon all over Eastern Asia.

(3) *Slow cooling and progressive reheating*. According to this path, the 10 °C/my cooling rate indicated by zircon and titanite U/Pb ages from the Jurassic granodiorite, is progressively modified since the Early Cretaceous by the continuous emplacement of large masses of granitic plutons that reheat the entire crust of the south-Liaodong peninsula area. This cooling path differs from the previous one in the sense that reheating might have started earlier in the beginning of Cretaceous as suggested by the bimodal distribution of pluton ages (Fig. 9 insert).

(4) *Two plutonic pulses*. During the Jurassic, after its emplacement, the granodiorite experienced a 10 °C/my cooling rate followed by a fast cooling rate at ca 40 °C/my at the end of the Jurassic that led to a rather "cool" crust. Then since the Early Cretaceous, the emplacement of a huge amount of granitic magma was responsible for reheating of the entire crust. This last possibility of cooling path of the south-Liaodong peninsula area is in agreement with the suggestion of lithosphere removal in the eastern NCC commencing in the Jurassic (Griffin et al., 1998; Gao et al., 2004). In this view, a Late Jurassic fast cooling rate similar to the early Cretaceous one must be taken into account. This cooling path is in agreement with the regional geology, since at the scale of NE China, the Mesozoic plutonism results in two distinct pulses, in the Jurassic and Cretaceous, respectively (Wu

et al., 2005a,b; Fig. 9). However, the tectonic setting of the Jurassic magmatism is not fully understood. Jurassic extensional tectonics might be assumed, on the basis of some grabens distributed in Liaoning Province (LBGMR, 1989). In this case, the Jurassic plutons might be interpreted as syn-kinematic bodies and a fast cooling rate will follow the emplacement of these plutons. Nevertheless, detail structural studies that could support this interpretation are not available yet. During the Early Cretaceous, the crust was progressively thinned and reheated due to the emplacement of the Early Cretaceous monzogranitic plutons and this event is coeval with extensional tectonics (Lin and Wang, 2006; Lin et al., 2008b).

No matter what cooling history is taken into consideration, our results indicate a rather complex tectonic evolution during the Late Jurassic to Early Cretaceous for the south-Liaodong peninsula area. Because extensional structures are not widespread developed despite the presence of some Jurassic basins, and the tectonic setting of the Jurassic plutons not fixed, the last possibility of two distinct thermal pulses (path 4) remains speculative (Fig. 9; LBGMR, 1989). The first and second ones (paths 1 and 2 in Fig. 9) imply the presence of a relatively "hot" crust and high heat flow during the entire Jurassic period. However, this is inconsistent with the recent evaluation of heat flow and thermal gradients that do not argue for "hot" Jurassic crust in north China (Zhai et al., 2004). In the Jurassic granodiorite, the garnet does not show any zonal structure, while allanite develops retrogressive zonation. This suggests that this granodiorite experienced a simple thermal evolution such as that depicted by path 3 in Fig. 9. Whatever the Late Jurassic-Early Cretaceous cooling path, a rapid cooling took place during the late Early Cretaceous, subsequent to the extensional emplacement of the monzogranitic plutons (116–122 Ma). A similar result was indicated by the Gudaoling syntectonic granite which is situated in the northern part of the south-Liaodong peninsula (Fig. 3; Yang et al., 2008). If path 3 is accepted, it reveals that, at least in the south-Liaodong peninsula area, extensional tectonics was not significant before the Early Cretaceous.

5.2. The significance of rapid exhumation and regional extension along the Eastern Margin of Eurasia

Previous structural studies show that the south-Liaodong peninsula massif is an asymmetric MCC with a NE–SW trending extension direction (Liu et al., 2005; Yang et al., 2007b; Lin et al., 2008b). Due to movements along detachment faults, the Jurassic granodioritic plutons, Paleoproterozoic and Archean country rocks were brought to the surface in the core of MCC. The $^{40}Ar/^{39}Ar$ ages constrain the date of the ductile extension around 120 Ma. These exhumed rocks record at least two different paths of cooling that are poorly documented in the other MCCs (Ratschbacher et al., 2000; Yang et al., 2007b). In the south-Liaodong peninsula MCC, these two different cooling histories correspond to different exhumation and geodynamic processes. The mechanism of lithosphere removal responsible for the Cretaceous reheating of the crust is still controversial (c.f. Lin and Wang, 2006 and references therein). The progressive thermo-mechanical convective ablation of the lithosphere, as suggested for the North American Cordilleras (Bird, 1979), was accepted by some workers (Griffin et al., 1998; Menzies and Xu, 1998; Xu, 2001). But such a mechanism cannot satisfactorily explain the peak of the magmatism and extensional structures such as MCC, syntectonic pluton, and half graben sedimentary basins of Early Cretaceous age (Fig. 10). Alternatively, another possible mechanism that can be invoked is the detachment of a large piece of lithosphere (Houseman et al., 1981). Because it answers many of the above questions about the thermal evolution of Eastern China, this lithosphere delamination model has been accepted by most of researchers (Deng et al., 1994, 1996; Wu et al., 2000, 2003; Gao et al., 1998, 2002). Nevertheless, whatever the model, the partial loss of lithospheric mantle would be also responsible for a significant uplift and rise of a high elevation plateau, like in Cenozoic Tibet (Turner et al., 1996). Although such a Cretaceous plateau is suggested for Mongolia and NE China (Meng et al., 2003), this topographic effect is not well recorded in the sedimentation since the amount of terrigeneous material deposited in the Cretaceous basins does not comply with the important erosion associated with such an uplift. The slow cooling history recorded by the Jurassic granodiorite also does not support the delamination model during the Jurassic (Griffin et al., 1998; Gao et al., 2004), at least in the Liaodong Peninsula area. As for the rapid cooling of the lithosphere, a detail discussion of the models of lithosphere removal is beyond the scope of this paper. Furthermore, the geodynamic cause of the Jurassic plutonism remains unsettled yet. Although an early extensional stage cannot be ruled out in the study area, strong evidence for such a Jurassic event is not documented. In the present state of knowledge, we consider that additional structural and cooling data on exhumed rocks from extensional domes are necessary to reach a satisfactory understanding of the geodynamic significance of the continental-scale Mesozoic extension in the North China Craton.

6. Conclusion

The south-Liaodong Peninsula MCC, which is the easternmost extensional dome recognized in China, provides a good example of synmetamorphic ductile shearing, syn-kinematic plutonism and polyphase exhumation. The Jurassic granodioritic plutons record two different phases of cooling. A slow cooling regime at about 3–10 °C/my before 122 Ma and a fast cooling rate of 40–55 °C/my after 122 Ma. This result indicates that the Jurassic granodiorite which occurs in the footwall of the detachment normal fault experienced two different exhumation processes during the Mesozoic: a Jurassic slow or negligible uplift, followed by a quite fast exhumation in the Cretaceous. These two different cooling histories probably correspond to a significant change of the geodynamic setting of Eastern China between the Jurassic and Cretaceous.

Acknowledgements

Field and laboratory expenses have been supported by a Knowledge Innovation Program of the Chinese Academy of Sciences (KZCX2-YW-Q05-05-03), and a NSFC grant (40872142, 90714007). Constructive comments by Drs. Simon Wilde, Pierre Vergely and Bin Chen on this draft are deeply acknowledged. We also thank Profs. Bor-ming Jahn and Wenjiao Xiao for their helpful editorial advices.

References

Allen, M.B., Macdonald, D.I., Zhao, X., Vincent, S., Brouet-Menzies, C., 1997. Early Cenozoic two-phase extension and late Cenozoic thermal subsidence and inversion of the Bohai Basin, Northern China. Marine and Petroleum Geology 14, 951–972.

Bird, P., 1979. Continental delamination and the Colorado plateau. Journal of Geophysical Research 84, 7561–7571.

Cheng, R.Y., Wu, F.Y., Ge, W., Sun, D., Liu, X., Yang, J., 2006. Emplacement age of the Raohe complex in eastern Heilongjiang province and the tectonic evolution of the eastern part of Northeastern China. Acta Petrologica Sinica 22, 315–325 (in Chinese with English abstract).

Dahl, P.S., 1996. The effects of composition on retentivity of argon and oxygen in hornblende and related amphiboles: a field-tested empirical model. Geochimica et Cosmochimica Acta 60, 3687–3700.

Davis, G.A., Zheng, Y., Wang, C., Darby, B.J., Zhang, Ch., Gehrels, G.E., 2001. Mesozoic tectonic evolution of the Yanshan fold and thrust belt, with emphasis on Hebei

and Liaoning provinces, northern China. In: Hendrix, M.S., Davis, G.A. (Eds.), Paleozoic and Mesozoic tectonic evolution of Central and Asia: From Continental Assembly to Intracontinental Deformation. Geological Society of American Memoir 194, Boulder, Colorado, pp. 171–194.

Deng, J., Mo, X., Zhao, H., Wu, Z., Luo, Z., Su, S., 2004. A new model for the dynamic evolution of Chinese lithosphere: 'continental roots-plume tectonics'. Earth Science Reviews 65, 223–275.

Deng, J., Zhao, H., Luo, Z., Guo, Z., Mo, X., 1998. Mantle plumes and lithosphere motion in East Asia. In: Flower, M.F.J., Chung, S.L., Lo, C.H., Lee, T.Y. (Eds.), Mantle Dynamics and Plate Interaction in East Asia, vol. 27. Geodynamics Series, pp. 59–66.

Deng, J.F., Mo, X.X., Zhao, H.L., Luo, Z.H., Du, Y.S., 1994. Lithosphere root/de-rooting and activation of the East China continent. Geoscience 8, 349–356 (in Chinese, with English abstract).

Deng, J.F., Zhao, H.L., Mo, X.X., 1996. Continental roots-plume tectonics of China: key to continental dynamics. Geological Publishing House, Beijing. pp. 1–110 (in Chinese, with English abstract).

Fan, W.M., Menzies, M.A., 1992. Destruction of aged lower lithosphere and asthenosphere mantle beneath eastern China. Geotectonica et Metallogenia 16, 171–179 (in Chinese with English abstract).

Faure, M., Lin, W., Monié, P., Bruguier, O., 2004. Paleoproterozoic collision tectonics in NE China: evidence for a 2Ga magmatic arc in Liaodong Peninsula. Terra Nova 16, 75–80.

Faure, M., Lin, W., Monié, P., Le Breton, N., Poussineau, S., Panis, D., Deloule, E., 2003a. Exhumation tectonics of the ultra high-pressure metamorphic rocks in the Qinling orogen in East China, new petrological-structural-radiometric insights from the Shandong peninsula. Tectonics 22, 1018–1039.

Faure, M., Lin, W., Scharer, U., Shu, L., Sun, Y., Arnaud, N., 2003b. Continental subduction and exhumation of UHP rocks, structural and geochronological insights from the Dabieshan (East China). Lithos 70, 213–241.

Faure, M., Trap, P., Lin, W., Monié, P., Bruguier, O., 2007. Polyorogenic evolution of the Paleoproterozoic Trans-North China Belt, new insights from the Lüliangshan- Hengshan-Wutaishan and Fuping massifs. Episodes 30, 95–106.

Fleck, R.J., Sutter, J.F., Elliot, D.H., 1977. Interpretation of discordant $^{40}Ar/^{39}Ar$ age-spectra of Mesozoic tholeiites from Antarctica. Geochimica et Cosmochimica Acta 41, 15–32.

Fu, M., Hu, Sh., Wang, J., 2005. Thermal regime transition in eastern North China and its tectonic implication. Science in China (Series D) 48, 840–848.

Gao, S., Rudnick, R.L., Yuan, H.L., Liu, X.M., Liu, Y.S., Xu, W.L., Ling, W.L., Ayers, J., Wang, X.C., Wang, Q.H., 2004. Recycling lower continental crust in the North China craton. Nature 432, 892–897.

Gao, S., Rudnick, R.L., Carlsonet, R.W., McDonough, W.F., Liu, Y.S., 2002. Re–Os evidence for replacement of ancient mantle lithosphere beneath the North China Craton. Earth and Planetary Science Letters 198, 307–322.

Gao, S., Zhang, B.-R., Jiu, Z.-M., Kern, H., Luo, T.-C., Zhao, Z.-D., 1998. How mafic is the lower continental crust? Earth and Planetary Science Letters 161, 101–117.

Griffin, W., Zhang, A., O'Reilly, S., Ryan, C.G., 1998. Phanerozoic evolution of the lithosphere beneath the Sino-Korean Craton. In: Flower, M.F.J., Chung, S.L., Lo, C.H., Lee, T.Y. (Eds.), Mantle Dynamics and Plate Interaction in East Asia, vol. 27. Geodynamics Series, pp. 107–126.

Hacker, B.R., Ratschbacher, L., Webb, L., Ireland, T., Walker, D., Dong, S., 1998. U/Pb zircon ages constrain the architecture of the ultrahigh-pressure Qinling-Dabie orogen, China. Earth and Planetary Science Letters 161, 215–230.

Hacker, B.R., Wallis, S.R., Ratschbacher, L., Grove, M., Gehrels, G., 2006. High-temperature geochronology constraints on the tectonic history and architecture of the ultrahigh-pressure Dabie–Sulu Orogen. Tectonics 25. doi:10.1029/2005TC001937.

Hammarstrom, J.M., Zen, E., 1986. Aluminum in hornblende: an empirical igneous geobarometer. American Mineralogist 71, 1297–1313.

Harrison, T.M., Duncan, I., McDougall, I., 1985. Diffusion of ^{40}Ar in biotite: temperature, pressure and compositional effects. Geochimica et Cosmochimica Acta 49, 2461–2468.

HBGMR (Hebei Bureau of Geology and Mineral Resources), 1989. Regional Geology of Hebei Province. Geological Publishing House, Beijing, 742 pp (in Chinese with English abstract).

Holdaway, M.J., 2000. Application of new experimental and garnet Margules data to the garnet–biotite geothermometer. American Mineralogist 85, 881–892.

Hollister, L.S., Grissom, G.C., Peters, E.K., Stowell, H.H., Sisson, V.B., 1987. Confirmation of solidification of calc-alkaline plutons. American Mineralogist 72, 231–239.

Houseman, G., McKenzie, D.P., Molnar, P., 1981. Convective instability of a thickened boundary layer and its relevance for the thermal evolution of continental convergent belts. Journal of Geophysical Research 86, 6115–6132.

Huang, T.K., 1945. On the major tectonic forms of China. Geological Memories, Series A 20, 1–165.

Jiang, N., Sun, Sh., Zhu, X., Mizuta, T., Ishiyama, D., 2003. Mobilization and enrichment of high-field strength elements during late- and post-magmatic processes in the Shuiquangou syenitic complex, Northern China. Chemical Geology 200, 117–128.

Johnson, M.C., Malcolm, J., Rutherford, J., 1989. Experimental calibration of the aluminum-in-hornblende-geobarometer with application to Long Valley caldera (California) volcanic rocks. Geology 17, 837–841.

Kohn, M.J., Spear, F.S., 1990. Two new geobarometers for garnet amphibolites, with application to southeastern Vermont. American Mineralogist 75, 89–96.

Krogh, T.E., 1982. Improved accuracy of U–Pb zircon ages by the creation of more concordant system using air abrasion technique. Geochimica et Cosmochimica Acta 46, 637–649.

Krogh-Ravna, E., 2000. Distribution of Fe^{2+} and Mg between coexisting garnet and hornblende in synthetic and natural systems: an empirical calibration of the garnet–hornblende Fe–Mg geothermometer. Lithos 53, 265–277.

Kusky, T.M., Li, J.H., 2003. Paleoproterozoic tectonic evolution of the North China Craton. Journal of Asian Earth Sciences 22, 383–397.

Lamb, M.A., Badarch, G., 1997. Paleozoic sedimentary basins and volcanic-arc systems of southern Mongolia: new stratigraphic and sedimentological constraints. International Geology Review 39, 542–576.

LBGMR (Liaoning Bureau of Geology and Mineral Resources), 1989. Regional Geology of Liaoning Province. Geological Publishing House, Beijing, 856 pp (in Chinese with English summary).

Leake, B.E., Woolley, A.R., Arps, C.E.S., Birch, W.D., Gilbert, M.C., Grice, J.D., Hawthorne, F.C., Kato, A., Kisch, H.J., Krivovichev, V.G., Laird, J., Mandarino, J.A., Maresch, W.V., Nickel, E.H., Rock, N.M.S., Schumacher, J.C., Smith, D.C., Stephenson, N.C.N., Ungaretti, L., Whittaker, E.J.W., Guo, Y., 1997. Nomenclature of amphiboles: report of the subcommittee on amphiboles of the international mineralogical association, commission on new minerals and mineral names. The Canadian Mineralogist 35, 219–246.

Li, S., Zhao, G., Sun, M., Han, Zh., Luo, Y., Hao, D., Xia, X., 2005. Deformation history of the Paleoproterozoic Liaohe assemblage in the eastern block of North China Craton. Journal of Asian Earth Sciences 24, 659–674.

Lin, W., Faure, M., Monié, P., Schärer, U., Zhang, L., Sun, Y., 2000. Tectonics of SE China, new insights from the Lushan massif (Jiangxi Province). Tectonics 19, 852–871.

Lin, W., Faure, M., Nomade, S., Shang, Q., Renne, P.R., 2008a. Permian-Triassic Amalgamation of Asia: insights from NE China sutures and their place in the final collision of North China and Siberia. Comptes Rendus Geoscience 340, 190–201.

Lin, W., Faure, M., Monie, P., Scharer, U., Panis, D., 2008b. Mesozoic extensional tectonics in Eastern margin of Eurasia continent, the case study of South-Liaodong peninsula dome, NE China. Journal of Geology 116, 134–154.

Lin, W., Wang, Q., 2006. Late Mesozoic extensional tectonics in North China Block – response to the lithosphere removal of North China Craton? Bulletin de la Société Géologique de France 177, 287–294.

Lister, G.S., Davis, G.A., 1989. The origin of metamorphic core complexes and detachment faults formed during Tertiary continental extension in the northern Colorado River region, USA. Journal Structural Geology 11, 65–94.

Liu, J., Davis, G., Lin, Z., Wu, F., 2005. The Liaonan metamorphic core complex, Southeastern Liaoning Province, North China: a likely contributor to Cretaceous rotation of Eastern Liaoning, Korea and contiguous areas. Tectonophysics 407, 65–80.

Lu, X., Wu, F., Lin, J., Sun, D., Zhang, Y., Guo, C., 2004. Geochronological successions of the Early Precambrian granitic magmatism in Southern Liaodong peninsula and it constraints on tectonic evolution of the north China Craton. Chinese Journal of Geology 39, 123–138 (in Chinese with English abstract).

Mattauer, M., Matte, P., Malavieille, J., Tapponnier, P., Maluski, H., Xu, Z., Lu, Y., Tang, Y., 1985. Tectonics of Qinling belt: Build-up and evolution of eastern Asia. Nature 317, 496–500.

McDougall, I., Harrison, T.M., 1999. Geochronology and Thermochronology by the $^{40}Ar/^{39}Ar$ Method. Oxford University Press, New York, Oxford, 269 pp.

Meng, Q., 2003. What drove late mesozoic extension of the northern China–Mongolia tract? Tectonophysics 369, 155–174.

Meng, Q., Hu, J., Jin, J., Zhang, Y., Xu, D., 2003. Tectonics of the late Mesozoic wide extension basin system in the China–Mongolia border region. Basin Research 15, 397–415.

Menzies, M.A., Xu, Y., 1998. Geodynamics of the North China Craton. In: Flower, M.F.J., Chung, S.L., Lo, C.H., Lee, T.Y. (Eds.), Mantle Dynamics and Plate Interaction in East Asia, vol. 27. Geodynamics Series, pp. 155–165.

Menzies, M.A., Fan, W.M., Zhang, M., 1993. Palaeozoic and Cenozoic lithoprobes and the loss of >120 km of Archean lithosphere, Sino-Korean craton, China. In: Prichard, H.M., Alabaster, T., Harris, N.B.W., Neary, C.R. (Eds.), Magmatic Processes and Plate Tectonics, vol. 76. Geological Society of London Special Publication, pp. 71–81.

Okada, H., 1999. Plume-related sedimentary basins in East Asia during the Cretaceous. Paleogeography, Paleoclimatology, Paleoecology 150, 1–11.

Okamoto, K., Maruyama, S., 1999. The high-pressure synthesis of lawsonite in the MORB + H_2O system. American Mineralogist 84, 362–373.

Ratschbacher, L., Hacker, B.R., Webb, L., McWilliams, M.O., Ireland, T., Dong, S., Calvert, A., Chateigner, D., Wenk, H., 2000. Exhumation of ultrahigh-pressure continental crust in east central China: cretaceous and cenozoic unroofing and the Tan-Lu fault. Journal of Geophysical Research 105, 13303–13338.

Ren, J., Kensaku, T., Li, S., Zhang, J., 2002. Late mesozoic and cenozoic rifting and its dynamic setting in Eastern China and adjacent areas. Tectonophysics 344, 175–205.

Samson, S.C., Alexander, E.C., 1987. Calibration of the inter laboratory $^{40}Ar/^{39}Ar$ dating standard MMHb-1. Chemical Geology 66, 27–34.

SBGMR (Shanxi Bureau of Geology and Mineral Resources), 1989. Regional Geology of Shanxi Province. Geological Publishing House, Beijing, 780 pp.

Schärer, U., 1984. The effect of initial ^{230}Th disequilibrium on young U–Pb ages, the Makalu case, Himalaya. Earth and Planetary Science Letters 67, 101–114.

Schärer, U., Labrousse, L., 2003. Dating the exhumation of UHP-rocks and associated crustal melting in the Norwegian Caledonides. Contributions to Mineralogy and Petrology 144, 758–770.

Schmidt, M.W., 1992. Amphibole composition in tonalite as a function of pressure: an experimental calibration of the Al-in-hornblende barometer. Contributions to Mineralogy and Petrology 110, 304–310.

Sengor, A.M.C., Natal'in, B.A., 1996. Paleotectonics of Asia: fragments of a synthesis. In: Yin, A., Harrison, T.M. (Eds.), The Tectonic Evolution of Asia. Cambridge University Press, pp. 486–641.

Shang, Q., 2004. Occurrences of Permian radiolarians in central and eastern Nei Mongol (Inner Mongolia) and their geological significance to the Northern China Orogen. Chinese Science Bulletin 49, 2613–2619.

Stacey, J.S., Kramers, J.D., 1975. Approximation of terrestrial lead isotope evolution by a two stage model. Earth and Planetary Science Letters 26, 207–221.

Tian, Z., Han, P., Xu, K., 1992. The Mesozoic–Cenozoic east China rift system. Tectonophysics 208, 341–363.

Trap, P., Faure, M., Lin, W., Monié, P., 2007. Late Paleoproterozoic (1900–1800 Ma) nappe stacking and polyphase deformation in the Hengshan-Wutaishan area: implications for the understanding of the Trans-North-China Belt, North China Craton. Precambrian Research 156, 85–106.

Turner, S., Arnaud, N., Liu, J., Rogers, N., Hawkesworth, C., Harris, N., Kelley, S., van Calsteren, P., Deng, W., 1996. Post-collision, shoshonitic volcanism on the Tibetan Plateau implications for convective thinning of the lithosphere and the source of ocean island basalts. Journal of Petrology 37, 45–71.

Wang, Q., Liu, X., 1986. Paleoplate tectonics between Cathaysia and Angaraland in Inner Mongolia of China. Tectonics 5, 1073–1088.

Wang, Y., Li, H., 2008. Initial formation and mesozoic tectonic exhumation of an intracontinental tectonic belt of the northern part of the Taihang mountain belt, Eastern Asia. The Journal of Geology 116, 155–172.

Wu, C.H., Zhang, J., Ren, L.D., 2004. Empirical garnet–biotite–plagioclase–quartz (GBPQ) geobarometry in medium- to high-grade metapelites. Journal of Petrology 45, 1907–1921.

Wu, F.Y., Yang, J.H., Zhang, Y.B., 2006. Emplacement ages of the mesozoic granites in southeastern part of the Western Liaoning Province. Acta Petrologica Sinica 22, 315–325 (in Chinese with English abstract).

Wu, F., Lin, J., Wilde, S.A., Zhang, X., Yang, J., 2005a. Nature and significance of the early cretaceous giant igneous event in eastern China. Earth and Planetary Science Letters 233, 103–119.

Wu, F., Yang, J., Wilde, S.A., Zhang, X., 2005b. Geochronology, petrogenesis and tectonic implications of the Jurassic granites in the Liaodong Peninsula, NE China. Chemical Geology 221, 127–156.

Wu, F.Y., Han, R.H., Yang, J.H., Wilde, S.A., Zhai, M.G., 2007. Initial constraints on granitic magmatism in North Korea using U–Pb zircon geochronology. Chemical Geology 238, 232–248.

Wu, F.Y., Jahn, B.M., Wilde, S.A., Sun, D.Y., 2000. Phanerozoic continental crustal growth: U–Pb and Sr–Nd isotopic evidence from the granites in northeastern China. Tectonophysics 328, 89–113.

Wu, F.Y., Jahn, B.M., Wilde, S.A., Lo, C.H., Yui, T.F., Lin, Q., Ge, W.C., 2003. Highly fractionated I-type granites in NE China (I): geochronology and petrogenesis. Lithos 66, 241–273.

Xiao, W., Windley, B.F., Hao, J., Zhai, M., 2003. Accretion leading to collision and the Permian Solonker suture, inner Mongolia, China: Termination of the Central Asian orogenic belt. Tectonics 22. doi:10.1029/2002TC001484.

Xu, Y.G., 2001. Thermo-tectonic destruction of the Archean lithospheric keel beneath the Sino-Korean craton in China: evidence, timing and mechanism. Physics and Chemistry of the Earth 26, 747–757.

Xu, Y.G., 1999. Roles of thermo-mechanic and chemical erosion in continental lithospheric thinning. Bulletin of Mineralogy Petrology and Geochemistry 18, 1–5 (in Chinese with English abstract).

Yang, J.H., Wu, F.Y., Chung, S.L., Lo, Ch.H., 2008. The extensional geodynamic setting of Early Cretaceous granitic intrusions in the eastern North China Craton: Evidence from laser ablation $^{40}Ar/^{39}Ar$ dating of K-bearing minerals. Acta Petrologica Sinica 24, 1175–1184 (in Chinese with English abstract).

Yang, J.H., Wu, F., Liu, X., Xie, L., Yang, Y., 2007a. Petrogenesis and geological significance of the Jurassic Xiaoheishan pluton in the Liaodong peninsula, East China: in-situ zircon U–Pb dating and Hf isotopic analysis. Bulletin of Mineralogy Petrology and Geochemistry 126, 29–43.

Yang, J.H., Wu, F.Y., Chung, S.L., Lo, Ch., Wilde, S.A., Davis, G.A., 2007b. Rapid exhumation and cooling of the Liaonan metamorphic core complex: Inferences from $^{40}Ar/^{39}Ar$ thermochronology and implications for Late Mesozoic extension in the eastern North China Craton. Geological Society of America Bulletin 119, 1405–1414.

Yang, J.H., Sun, J.F., Chen, F.K., Wilde, S.A., Wu, F.Y., 2007c. Sources and petrogenesis of Late Triassic dolerite dikes in the Liaodong Peninsula: implications for post-collisional lithosphere thinning of Eastern North China Craton. Journal of Petrology 48, 1973–1997.

Yang, J.H., Wu, F.Y., Shao, J.A., Xie, L., Liu, X., 2006. In-situ U–Pb dating and Hf isotopic analyses of zircon from volcanic rocks of the Houcheng and Zhangjiakou formations in the Zhang-Xuan area, Northeast China. Earth Science – Journal of China University of Geosciences 31, 71–80 (in Chinese with English abstract).

Yang, J.H., Wu, F.Y., Lo, Ch.H., Chung, S.L., Zhang, Y.B., Wilde, S.A., 2004. Deformation age of Jurassic granites in the Dandong area, eastern China: $^{40}Ar/^{39}Ar$ geochronological constraints. Acta Petrologica Sinica 20, 1205–1214 (in Chinese with English abstract).

Yin, A., Nie, S., 1993. An indentation model for the North and South China collision and the development of the Tan-lu and normal fault systems, Eastern Asia. Tectonics 12, 801–813.

Yin, A., Nie, S., 1996. A Phanerozoic palinspastic reconstruction of China and its neighboring regions. In: Yin, A., Harrison, T.M. (Eds.), The Tectonic Evolution of Asia. Cambridge University Press, pp. 442–485.

Zartman, R.E., Doe, B.R., 1981. Plumbotectonics, the model. Tectonophysics 75, 135–162.

Zhai, M., Zhu, R., Liu, J., Meng, Q., Hou, Q., Hu, S., Liu, W., Li, Zh., Zhang, H., 2004. Time range of mesozoic tectonic regime inversion in eastern North China Block. Science in China (Series D) 47, 151–159.

Zhang, H.F., 2005. Transformation of lithospheric mantle through peridotite-melt reaction: A case of Sino-Korean craton. Earth and Planetary Science Letters 237, 768–780.

Zhang, H.F., Zheng, J.P., 2003. Geochemical characteristics and petrogenesis of Mesozoic basalts from the North China Craton: a case study in Fuxin, Liaoning Province. Chinese Science Bulletin 48, 924–930.

Zhang, H.F., Sun, M., 2002. Geochemistry of Mesozoic basalts and mafic dikes in southeastern North China craton, and tectonic implication. International Geological Review 44, 370–382.

Zhang, L.S., Schärer, U., 1996. Inherited Pb components in magmatic titanite and their consequence for the interpretation of U–Pb ages. Earth and Planetary Science Letters 138, 57–65.

Zhao, G., Sun, M., Wilde, S.A., Li, S.Z., 2005. Late Archean to Paleoproterozoic evolution of the North China Craton: key issues revisited. Precambrian Research 136, 177–202.

Zheng, X., 1997. Characteristics and geological significance of deep tectonics in Liaoning Province. Liaoning Geology 3, 16–38.

Zorin, Y.A., 1999. Geodynamics of the western part of the Mongolia-Okhotsk collisional belt, Trans-Baikal region (Russia) and Mongolia. Tectonophysics 306, 33–56.